

Euler inversion: Locating sources of potential-field data through inversion of Euler's homogeneity equation

Leonardo Uieda¹, Gelson Ferreira Souza-Junior¹, India Uppal², Vanderlei Coelho Oliveira Jr.³

¹ Universidade de São Paulo, Brazil; ² University of Liverpool, UK; ³ Observatório Nacional, Brazil;

Submitted for publication to *Geophysical Journal International* on 2024/12/20.

Keywords: Gravity anomalies and Earth structure; Magnetic anomalies: modelling and interpretation; Inverse theory;

¹ Abstract

² Locating the sources of observed disturbances in potential-field data is a challenging problem
³ due to the non-unique nature of the inverse problem. The Euler deconvolution method was
⁴ created to solve this issue, particularly for idealized sources (such as spheres, planar vertical
⁵ dykes). Euler deconvolution has become widely used in potential-field methods due, in large
⁶ part, to its low computational cost and ease of implementation into software. However, it is
⁷ widely known that Euler deconvolution suffers from some shortcomings: 1) non-uniqueness of
⁸ the solution with respect to the depth of the source and the structural index (a parameter that
⁹ represents the idealised shape of the source); 2) sensitivity to short-wavelength noise in the data
¹⁰ derivatives which are used as inputs for the method. Here, we present a new method called *Euler*
¹¹ *inversion* which is a reformulation of the inverse problem of Euler's homogeneity equation as an
¹² implicit mathematical model rather than a parametric one. Euler inversion is a constrained, non-
¹³ linear inverse problem capable of estimating both the model parameters (location of the source
¹⁴ and constant base level) and the predicted data (potential field and its derivatives). We show
¹⁵ that Euler inversion is less sensitive than Euler deconvolution to short-wavelength noise and to
¹⁶ the presence of interfering sources in the data window. By also estimating the predicted data,
¹⁷ Euler inversion is also able to estimate the integer structural index because the data misfit is

¹⁸ smaller when the correct structural index is used for the inversion. Furthermore, most matrices
¹⁹ involved in the method are either sparse or diagonal, making Euler inversion computationally
²⁰ efficient. Tests on synthetic data and a real aeromagnetic dataset from Rio de Janeiro, Brazil,
²¹ demonstrate the effectiveness of Euler inversion to delineate sources with variable geometries
²² and correctly estimate their depths.

²³ 1 Introduction

²⁴ Estimating the depths of the sources of measured anomalies is a common challenge in potential-
²⁵ field geophysics. One of the most widely used techniques for providing depth estimates is Euler
²⁶ deconvolution ([Reid et al., 1990](#); [Thompson, 1982](#)). Its widespread adoption is due, in large
²⁷ part, to its low algorithmic complexity and fast computation times, both of which are orders of
²⁸ magnitude smaller than solutions from 3D inverse problems. As a result, Euler deconvolution
²⁹ is widely available in both commercial and open-source software ([Uieda et al., 2013, 2014](#)).
³⁰ Unfortunately, this popularity has also led to abuses of the method, as reported in [Reid and](#)
³¹ [Thurston \(2014\)](#) and [Reid et al. \(2014\)](#).

³² Euler deconvolution is based on a least-squares solution to Euler's homogeneity equation for
³³ idealised sources. The method estimates the coordinates of a source of potential-field anomalies,
³⁴ as well as a constant shift in the data, known as a base level. The source geometry is described
³⁵ by a parameter called the structural index, which must be an integer to have physical meaning
³⁶ ([Reid and Thurston, 2014](#); [Stavrev and Reid, 2007](#)). The inputs for Euler deconvolution are the
³⁷ potential-field data, its three spatial derivatives, and the structural index. The least-squares
³⁸ inversion is then performed multiple times in a moving window scheme in order to estimate
³⁹ coordinates for the multiple sources that are usually present in a dataset.

⁴⁰ It is well known that Euler deconvolution suffers from some limitations, of which we highlight:

- ⁴¹ 1. **Separation of reliable and spurious solutions:** The moving window procedure
⁴² adopted in Euler deconvolution generates many estimated positions which are consid-
⁴³ ered spurious and must be removed. Spurious solutions happen when the moving window

44 does not contain any anomalies or only contains parts of an anomaly. FitzGerald et al.
45 (2004) and Melo and Barbosa (2020) provide overviews of the many existing methods that
46 have been developed to remove spurious solutions.

47 **2. Sensitivity to high-frequency noise:** Random noise in the data is usually of high-
48 frequency, which gets amplified in the derivative calculations. Since the field derivatives
49 are used in the Jacobian matrix of the least-squares problem, errors in the derivatives
50 will have a large impact on the solution. Pateka et al. (2009), Saleh and Pateka (2012),
51 and Florio et al. (2014) recommend using regularised derivatives or other smoothing tech-
52 niques to reduce the noise amplification and obtain more reliable solutions. This is also
53 why Euler deconvolution variants that rely on higher-order derivatives, like tilt-Euler de-
54 convolution (Huang et al., 2019; Salem et al., 2007) and AN-EUL (Salem and Ravat,
55 2003), present a larger dispersion of estimated positions and are more sensitive to noise
56 in general. Methods like finite-difference Euler deconvolution (Gerovska et al., 2005) and
57 ratio-Euler deconvolution (Huang et al., 2022) were specifically developed to avoid the use
58 of higher-order derivatives because of this noise-sensitivity issue.

59 **3. Correlation of the estimated depth and the structural index:** Silva et al. (2001)
60 demonstrated theoretically and in practice that the estimated depth from Euler decon-
61 volution is directly correlated with the structural index used. The higher the structural
62 index, the larger the estimated depth. This makes it very important to know the correct
63 structural index for the type of source being interpreted. Some Euler deconvolution vari-
64 ants have been developed that are able to estimate the structural index (e.g., Florio and
65 Fedi, 2013; Florio et al., 2014; Gerovska et al., 2005; Melo and Barbosa, 2018; Melo et al.,
66 2013; Salem and Ravat, 2003; Salem et al., 2007; Silva and Barbosa, 2003). However, most
67 of these methods estimate real-valued structural indices instead of integers, are sensitive
68 to noise, and tend to underestimate the structural index under realistic noise and signal
69 overlap scenarios.

70 We aim to tackle the issues of sensitivity to noise and structural index estimation by re-
71 formulating the inverse problem of solving Euler's homogeneity equation. The issue of noise

72 sensitivity can be traced back to the presence of data derivatives in the Jacobian matrix, which
73 generally contain larger amounts of noise than the original potential field. We propose formulating
74 the inverse problem as a non-linear optimisation with Euler's equation as a constraint. This
75 is similar to "total least-squares" in statistics (Van Huffel and Vandewalle, 1991) and "combined
76 adjustment" in geodesy (Vanícek and Krakiwsky, 1986). Another advantage of this new formu-
77 lation is the ability to calculate predicted data for the potential-field and its three derivatives,
78 which is impossible in Euler deconvolution and all of its variants. We call our new method
79 "Euler inversion".

80 2 Methodology

81 Starting with Thompson (1982) and Reid et al. (1990), Euler's equation has been used to
82 estimate the source positions of gravity and magnetic data. In this section, we will review
83 the solution of Euler's equation for the source location (x_o, y_o, z_o) by Euler deconvolution (Reid
84 et al., 1990) and then present a new method, called *Euler inversion*, for solving Euler's equation
85 using total least-squares.

86 We start with Euler's homogeneity equation

$$(x - x_o)\partial_x f + (y - y_o)\partial_y f + (z - z_o)\partial_z f + \eta(f - b) = 0 , \quad (1)$$

87 in which f is a homogeneous function (in this case, a potential-field), ∂_α is the derivative
88 operator in the α dimension, (x, y, z) are the coordinates of the observation point, (x_o, y_o, z_o)
89 are the coordinates of the field source, b is the base level representing a constant shift in the
90 field, and η is the structural index, which is related to the nature of the source and how its
91 potential-field values decay with distance (Reid and Thurston, 2014; Ruddock et al., 1966). The
92 coordinate system is defined with x pointing eastward, y pointing northward, and z pointing
93 upward. Equation 1 relates the coordinates of the source with the potential field and its gradient
94 observed at the point (x, y, z) .

95 Given N observations points in which we have measured f and its gradient (for a total $4N$

96 data), we can define the system of N equations and 4 unknowns

$$\begin{aligned}
 (x_1 - x_o)\partial_x f_1 + (y_1 - y_o)\partial_y f_1 + (z_1 - z_o)\partial_z f_1 + \eta(f_1 - b) &= 0 \\
 (x_2 - x_o)\partial_x f_2 + (y_2 - y_o)\partial_y f_2 + (z_2 - z_o)\partial_z f_2 + \eta(f_2 - b) &= 0 \\
 &\vdots \\
 (x_N - x_o)\partial_x f_N + (y_N - y_o)\partial_y f_N + (z_N - z_o)\partial_z f_N + \eta(f_N - b) &= 0
 \end{aligned} \tag{2}$$

97 Both Euler deconvolution and Euler inversion aim to solve the equation system above to estimate
98 the parameter vector

$$\mathbf{p} = \begin{bmatrix} x_o & y_o & z_o & b \end{bmatrix}^T. \tag{3}$$

99 2.1 Euler deconvolution

100 Euler deconvolution starts by rearranging Equation 2 to place the parameters on the left-hand
101 side and all other terms on the right-hand side. This is an attempt to form a *parametric model*
102 which results in the equation system

$$\begin{aligned}
 -x_o\partial_x f_1 - y_o\partial_y f_1 - z_o\partial_z f_1 - \eta b &= -x_1\partial_x f_1 - y_1\partial_y f_1 - z_1\partial_z f_1 - \eta f_1 \\
 -x_o\partial_x f_2 - y_o\partial_y f_2 - z_o\partial_z f_2 - \eta b &= -x_2\partial_x f_2 - y_2\partial_y f_2 - z_2\partial_z f_2 - \eta f_2 \\
 &\vdots \\
 -x_o\partial_x f_N - y_o\partial_y f_N - z_o\partial_z f_N - \eta b &= -x_N\partial_x f_N - y_N\partial_y f_N - z_N\partial_z f_N - \eta f_N
 \end{aligned} \tag{4}$$

103 which can be written in matrix form as

$$\underbrace{\begin{bmatrix} -\partial_x f_1 & -\partial_y f_1 & -\partial_z f_1 & -\eta \\ -\partial_x f_2 & -\partial_y f_2 & -\partial_z f_2 & -\eta \\ \vdots & \vdots & \vdots & \vdots \\ -\partial_x f_N & -\partial_y f_N & -\partial_z f_N & -\eta \end{bmatrix}}_{\mathbf{A}} \underbrace{\begin{bmatrix} x_o \\ y_o \\ z_o \\ b \end{bmatrix}}_{\mathbf{p}} = \underbrace{\begin{bmatrix} -x_1\partial_x f_1 - y_1\partial_y f_1 - z_1\partial_z f_1 - \eta f_1 \\ -x_2\partial_x f_2 - y_2\partial_y f_2 - z_2\partial_z f_2 - \eta f_2 \\ \vdots \\ -x_N\partial_x f_N - y_N\partial_y f_N - z_N\partial_z f_N - \eta f_N \end{bmatrix}}_{\mathbf{c}}, \tag{5}$$

¹⁰⁴ in which \mathbf{A} is the Jacobian matrix of Euler's equation (Equation 1) concerning the parameters
¹⁰⁵ (Equations 3) and \mathbf{c} is a *pseudo-data vector*.

¹⁰⁶ The solution proposed by [Thompson \(1982\)](#) and [Reid et al. \(1990\)](#) is a least-squares estimate
¹⁰⁷ of \mathbf{p}

$$\hat{\mathbf{p}} = (\mathbf{A}^T \mathbf{A})^{-1} \mathbf{A}^T \mathbf{c} . \quad (6)$$

¹⁰⁸ The covariance matrix of the solution \mathbf{C}_p is obtained through standard error propagation as-
¹⁰⁹ suming that the only variable with uncertainty is the pseudo-data vector \mathbf{c}

$$\mathbf{C}_p = \hat{\sigma}_0^2 (\mathbf{A}^T \mathbf{A})^{-1} , \quad (7)$$

¹¹⁰ in which $\hat{\sigma}_0^2 = \|\mathbf{c} - \mathbf{Ap}\|^2/(N - 4)$ is the reduced chi-squared statistic and an estimate of the
¹¹¹ variance factor of \mathbf{c} .

¹¹² The solution in Equation 6 above is valid only if the contents of the Jacobian matrix \mathbf{A} are
¹¹³ assumed to be error-free. As can be seen from Equation 5, the Jacobian contains the derivatives
¹¹⁴ of f , which are often computed numerically by finite-differences or Fourier transforms and
¹¹⁵ are known to amplify the high-frequency random noise in the data. This presents a problem,
¹¹⁶ particularly for the estimation of z_o , which has been widely explored in the literature ([Florio](#)
¹¹⁷ [et al., 2014](#); [Melo and Barbosa, 2020](#); [Pateka et al., 2009](#); [Silva et al., 2001](#)).

¹¹⁸ 2.2 Euler inversion: Formulation

¹¹⁹ Euler inversion starts by assigning the potential-field f to a $N \times 1$ vector

$$\mathbf{f} = \begin{bmatrix} f_1 & f_2 & \cdots & f_N \end{bmatrix}^T . \quad (8)$$

¹²⁰ We can then define a $4N \times 1$ *data vector* which contains all of the values of f and its gradient

$$\mathbf{d} = \begin{bmatrix} \mathbf{f}^T & \nabla_x \mathbf{f}^T & \nabla_y \mathbf{f}^T & \nabla_z \mathbf{f}^T \end{bmatrix}^T . \quad (9)$$

121 in which ∇_α is the gradient operator in the α dimension.

122 Next, we formulate the $N \times 4$ equation system from Euler's equation (Equation 2) as a
123 non-linear function of both parameters and data

$$\mathbf{e}(\mathbf{p}, \mathbf{d}) = \mathbf{0} , \quad (10)$$

124 which is known in geodesy as an *implicit mathematical model* (Vanícek and Krakiwsky, 1986).

125 We then wish to solve the following constrained optimisation problem with non-linear equal-
126 ity constraints to estimate both the parameters and the predicted data simultaneously

$$\begin{aligned} \min_{\mathbf{p}, \mathbf{d}} \quad & \phi(\mathbf{d}) = [\mathbf{d}^o - \mathbf{d}]^T \mathbf{W} [\mathbf{d}^o - \mathbf{d}] \\ \text{subject to} \quad & \mathbf{e}(\mathbf{p}, \mathbf{d}) = \mathbf{0} , \end{aligned} \quad (11)$$

127 in which \mathbf{d}^o is the *observed data vector* which contains all of the $4N$ observations of f and
128 its gradient, \mathbf{d} is the *predicted data vector* from Equation 9, and \mathbf{W} is a $4N \times 4N$ diagonal
129 weight matrix. The first N terms of the diagonal of \mathbf{W} are the weights for the potential field
130 observations and the following $3N$ terms are the weights of x-, y-, and z-derivatives of the
131 potential field, in order.

132 The constrained problem in Equation 11 can be transformed into an unconstrained problem
133 by using the Lagrangian

$$\mathcal{L}(\mathbf{p}, \mathbf{d}, \boldsymbol{\lambda}) = [\mathbf{d}^o - \mathbf{d}]^T \mathbf{W} [\mathbf{d}^o - \mathbf{d}] + 2\boldsymbol{\lambda}^T \mathbf{e} , \quad (12)$$

134 in which $\boldsymbol{\lambda}$ is an $N \times 1$ vector of Lagrange multipliers. The non-linear Lagrangian is minimised
135 through Newton's method (Aster et al., 2018). We start with initial estimates \mathbf{p}_0 and \mathbf{d}_0 and
136 then iteratively apply corrections $\Delta\mathbf{p}_k$ and $\Delta\mathbf{d}_k$ until convergence is achieved. To calculate
137 the corrections, we introduce a new variable $\mathbf{u} = [\mathbf{d}^T \ \boldsymbol{\lambda}^T \ \mathbf{p}^T]^T$, expand the Lagrangian $\mathcal{L}(\mathbf{u})$
138 (Equation 12) in a Taylor series around point \mathbf{u}_k , and disregard terms of order higher than two

$$\mathcal{L}(\mathbf{u}) \approx \Gamma(\mathbf{u}) = \mathcal{L}(\mathbf{u}_k) + \Delta\mathbf{u}_k^T \nabla \mathcal{L}(\mathbf{u}_k) + \frac{1}{2} \Delta\mathbf{u}_k^T \mathbf{H}_k \Delta\mathbf{u}_k , \quad (13)$$

¹³⁹ in which ∇ is the gradient operator and \mathbf{H}_k is the Hessian matrix of \mathcal{L} evaluated at \mathbf{u}_k . Equation ¹⁴⁰ 13 is a quadratic function of $\Delta\mathbf{u}_k$ and we can obtain its minimum by taking its gradient ¹⁴¹ and equating it to the null vector

$$\begin{aligned}\nabla\Gamma(\Delta\mathbf{u}_k) &= \nabla\mathcal{L}(\mathbf{u}_k) + \mathbf{H}_k\Delta\mathbf{u}_k = \mathbf{0} , \\ \mathbf{H}_k\Delta\mathbf{u}_k &= -\nabla\mathcal{L}(\mathbf{u}_k) .\end{aligned}\quad (14)$$

¹⁴² The equation above is the *system of normal equations*, which can also be written in terms of \mathbf{p} , ¹⁴³ $\boldsymbol{\lambda}$, and \mathbf{d}

$$\underbrace{\begin{bmatrix} \mathbf{H}_k^{dd} & \mathbf{H}_k^{d\lambda} & \mathbf{H}_k^{dp} \\ \mathbf{H}_k^{\lambda d} & \mathbf{H}_k^{\lambda\lambda} & \mathbf{H}_k^{\lambda p} \\ \mathbf{H}_k^{pd} & \mathbf{H}_k^{p\lambda} & \mathbf{H}_k^{pp} \end{bmatrix}}_{\text{Hessian of } \mathcal{L}} \underbrace{\begin{bmatrix} \Delta\mathbf{d}_k \\ \Delta\boldsymbol{\lambda}_k \\ \Delta\mathbf{p}_k \end{bmatrix}}_{\Delta\mathbf{u}_k} = -\underbrace{\begin{bmatrix} \nabla_d\mathcal{L}(\mathbf{p}_k, \mathbf{d}_k, \boldsymbol{\lambda}_k) \\ \nabla_\lambda\mathcal{L}(\mathbf{p}_k, \mathbf{d}_k, \boldsymbol{\lambda}_k) \\ \nabla_p\mathcal{L}(\mathbf{p}_k, \mathbf{d}_k, \boldsymbol{\lambda}_k) \end{bmatrix}}_{\text{gradient of } \mathcal{L}}, \quad (15)$$

¹⁴⁴ in which ∇_α is the gradient operator with respect to variable α and $\mathbf{H}_k^{\alpha\beta}$ is the Hessian matrix ¹⁴⁵ of \mathcal{L} with respect to variables α and β , evaluated at \mathbf{u}_k . Since the order of derivation can be ¹⁴⁶ swapped in the Hessian matrices and the Hessian of \mathcal{L} is symmetric, the above equation can be ¹⁴⁷ simplified to

$$\begin{bmatrix} \mathbf{H}_k^{dd} & \mathbf{H}_k^{d\lambda} & \mathbf{H}_k^{dp} \\ \mathbf{H}_k^{d\lambda T} & \mathbf{H}_k^{\lambda\lambda} & \mathbf{H}_k^{\lambda p} \\ \mathbf{H}_k^{dp T} & \mathbf{H}_k^{\lambda p T} & \mathbf{H}_k^{pp} \end{bmatrix} \begin{bmatrix} \Delta\mathbf{d}_k \\ \Delta\boldsymbol{\lambda}_k \\ \Delta\mathbf{p}_k \end{bmatrix} = -\begin{bmatrix} \nabla_d\mathcal{L}(\mathbf{p}_k, \mathbf{d}_k, \boldsymbol{\lambda}_k) \\ \nabla_\lambda\mathcal{L}(\mathbf{p}_k, \mathbf{d}_k, \boldsymbol{\lambda}_k) \\ \nabla_p\mathcal{L}(\mathbf{p}_k, \mathbf{d}_k, \boldsymbol{\lambda}_k) \end{bmatrix} . \quad (16)$$

¹⁴⁸ Now, we must derive the three gradient vectors and six Hessian matrices in Equation ¹⁴⁹ 16. We will start with the gradient vectors.

$$\begin{aligned}\nabla_d\mathcal{L}(\mathbf{p}_k, \mathbf{d}_k, \boldsymbol{\lambda}_k) &= 2(-\mathbf{W}[\mathbf{d}^o - \mathbf{d}_k] + \mathbf{B}_k^T\boldsymbol{\lambda}_k) , \\ \nabla_\lambda\mathcal{L}(\mathbf{p}_k, \mathbf{d}_k, \boldsymbol{\lambda}_k) &= 2\mathbf{e}_k , \\ \nabla_p\mathcal{L}(\mathbf{p}_k, \mathbf{d}_k, \boldsymbol{\lambda}_k) &= 2\mathbf{A}_k^T\boldsymbol{\lambda}_k ,\end{aligned}\quad (17)$$

¹⁵⁰ in which $\mathbf{e}_k = \mathbf{e}(\mathbf{p}_k, \mathbf{d}_k)$ (Equation 10), \mathbf{A}_k is the $N \times 4$ *parameter Jacobian* matrix of Euler's ¹⁵¹ equation (Equation 5) evaluated on $(\mathbf{p}_k, \mathbf{d}_k)$, and \mathbf{B}_k is the $N \times 4N$ *data Jacobian* of Euler's

equation, also evaluated on $(\mathbf{p}_k, \mathbf{d}_k)$. The data Jacobian \mathbf{B}_k contains the first derivatives of Euler's equation (Equation 1) with respect to the data vector \mathbf{d} (Equation 9). It is composed of four diagonal matrices

$$\mathbf{B}_k = \begin{bmatrix} \mathbf{B}_k^f & \mathbf{B}_k^x & \mathbf{B}_k^y & \mathbf{B}_k^z \end{bmatrix} . \quad (18)$$

The diagonal elements of each of the four matrices are

$$B_{kii}^f = \eta , \quad B_{kii}^x = x_i - x_{ok} , \quad B_{kii}^y = y_i - y_{ok} , \quad B_{kii}^z = z_i - z_{ok} . \quad (19)$$

The Hessian matrices are calculated using a Gauss-Newton approximation disregarding second-order derivatives. The six independent Hessians are given by

$$\begin{aligned} \mathbf{H}_k^{dd} &\approx 2\mathbf{W} , \quad \mathbf{H}_k^{\lambda\lambda} = \mathbf{0} , \quad \mathbf{H}_k^{pp} \approx \mathbf{0} , \\ \mathbf{H}_k^{d\lambda} &= 2\mathbf{B}^T , \quad \mathbf{H}_k^{\lambda p} = 2\mathbf{A} , \quad \mathbf{H}_k^{dp} \approx \mathbf{0} . \end{aligned} \quad (20)$$

Substituting the gradients (Equation 17) and Hessians (Equation 20) into the system of normal equations of Newton's method (Equation 16) we arrive at

$$\begin{bmatrix} \mathbf{W} & \mathbf{B}_k^T & \mathbf{0} \\ \mathbf{B}_k & \mathbf{0} & \mathbf{A}_k \\ \mathbf{0} & \mathbf{A}_k^T & \mathbf{0} \end{bmatrix} \begin{bmatrix} \Delta\mathbf{d}_k \\ \Delta\boldsymbol{\lambda}_k \\ \Delta\mathbf{p}_k \end{bmatrix} = - \begin{bmatrix} -\mathbf{W}[\mathbf{d}^o - \mathbf{d}_k] + \mathbf{B}_k^T\boldsymbol{\lambda}_k \\ \mathbf{e}_k \\ \mathbf{A}_k^T\boldsymbol{\lambda}_k \end{bmatrix} . \quad (21)$$

Since the data weight matrix \mathbf{W} is diagonal and invertible, we can use the following identity to eliminate one equation from the equation system above (Wells and Krakiwsky, 1971)

$$\begin{bmatrix} \mathbf{C} & \mathbf{D} \\ \mathbf{E} & \mathbf{F} \end{bmatrix} \begin{bmatrix} \mathbf{g} \\ \mathbf{h} \end{bmatrix} + \begin{bmatrix} \mathbf{t} \\ \mathbf{v} \end{bmatrix} = \begin{bmatrix} \mathbf{0} \\ \mathbf{0} \end{bmatrix} \Rightarrow [\mathbf{F} - \mathbf{E}\mathbf{C}^{-1}\mathbf{D}] \mathbf{h} + \mathbf{v} - \mathbf{E}\mathbf{C}^{-1}\mathbf{t} = \mathbf{0} . \quad (22)$$

Applying the identity to Equation 21 with $\mathbf{g} = \Delta\mathbf{d}_k$ and $\mathbf{h} = [\Delta\boldsymbol{\lambda}_k \quad \Delta\mathbf{p}_k]^T$ leads to

$$\begin{bmatrix} -\mathbf{Q}_k & \mathbf{A}_k \\ \mathbf{A}_k^T & \mathbf{0} \end{bmatrix} \begin{bmatrix} \Delta\boldsymbol{\lambda}_k \\ \Delta\mathbf{p}_k \end{bmatrix} + \begin{bmatrix} \mathbf{e}_k + \mathbf{B}_k\mathbf{r}_k - \mathbf{Q}_k\boldsymbol{\lambda}_k \\ \mathbf{A}_k^T\boldsymbol{\lambda}_k \end{bmatrix} = \begin{bmatrix} \mathbf{0} \\ \mathbf{0} \end{bmatrix} . \quad (23)$$

¹⁶³ in which $\mathbf{Q}_k = \mathbf{B}_k \mathbf{W}^{-1} \mathbf{B}_k^T$ and $\mathbf{r}_k = [\mathbf{d}^o - \mathbf{d}_k]$ is the residual vector. Applying the identity once
¹⁶⁴ more to the equation system above leads to a solution for the parameter correction vector

$$\hat{\Delta}\mathbf{p}_k = -[\mathbf{A}_k^T \mathbf{Q}_k^{-1} \mathbf{A}_k]^{-1} \mathbf{A}_k^T \mathbf{Q}_k^{-1} [\mathbf{B}_k \mathbf{r}_k + \mathbf{e}_k] . \quad (24)$$

¹⁶⁵ We can obtain an expression for $\hat{\Delta}\boldsymbol{\lambda}_k$ as a function of $\hat{\Delta}\mathbf{p}_k$ from Equation 23, which results
¹⁶⁶ in

$$\hat{\Delta}\boldsymbol{\lambda}_k = \mathbf{Q}_k^{-1} [\mathbf{A}_k^T \hat{\Delta}\mathbf{p}_k + \mathbf{B}_k \mathbf{r}_k + \mathbf{e}_k] - \boldsymbol{\lambda}_k . \quad (25)$$

¹⁶⁷ Finally, we can substitute the expression above into the first equation of the system of normal
¹⁶⁸ equations (Equation 21) to obtain the data correction as a function of $\hat{\Delta}\mathbf{p}_k$

$$\hat{\Delta}\mathbf{d}_k = \mathbf{r}_k - \mathbf{W}^{-1} \mathbf{B}_k^T \mathbf{Q}_k^{-1} [\mathbf{A}_k^T \hat{\Delta}\mathbf{p}_k + \mathbf{B}_k \mathbf{r}_k + \mathbf{e}_k] . \quad (26)$$

¹⁶⁹ The covariance matrix of \mathbf{p} is used to rank and filter solutions during the moving window
¹⁷⁰ procedure. It can be estimated by propagating uncertainties from the observed data \mathbf{d}^o to
¹⁷¹ the parameter correction vector (Equation 24) and, hence, to the parameter vector (Wells and
¹⁷² Krakiwsky, 1971). The covariance matrix of the observed data is approximated by $\mathbf{C}_d = \hat{\sigma}_0^2 \mathbf{W}^{-1}$.
¹⁷³ Recalling that matrix \mathbf{Q} is diagonal, the parameter covariance matrix is estimated at the last
¹⁷⁴ iteration of the Gauss-Newton method (iteration L) as

$$\begin{aligned} \mathbf{C}_p &= [\mathbf{A}_L^T \mathbf{Q}_L^{-1} \mathbf{A}_L]^{-1} \mathbf{A}_L^T \mathbf{Q}_L^{-1} \mathbf{B}_L \mathbf{C}_d \mathbf{B}_L^T \mathbf{Q}_L^{-1} \mathbf{A}_L [\mathbf{A}_L^T \mathbf{Q}_L^{-1} \mathbf{A}_L]^{-1} , \\ &= \hat{\sigma}_0^2 [\mathbf{A}_L^T \mathbf{Q}_L^{-1} \mathbf{A}_L]^{-1} , \end{aligned} \quad (27)$$

¹⁷⁵ in which $\hat{\sigma}_0^2 = \|\mathbf{d}^o - \mathbf{d}_L\|^2 / (4N - 4)$ is the reduced chi-squared statistic of the Euler inversion
¹⁷⁶ and an estimate of the variance factor of the observed data \mathbf{d}^o .

¹⁷⁷ **2.3 Euler inversion: Practical implementation**

¹⁷⁸ **2.3.1 Initial estimates and convergence**

¹⁷⁹ Unlike a traditional Gauss-Newton inversion of a parametric model, the Euler inversion pro-
¹⁸⁰ cedure estimates corrections to both the parameter vector \mathbf{p} and the predicted data vector \mathbf{d}
¹⁸¹ at each iteration. Hence, the optimisation requires initial values for both the parameters and
¹⁸² the predicted data. The initial value of the parameters is taken as the solution of traditional
¹⁸³ Euler deconvolution $\mathbf{p}_0 = [\mathbf{A}^T \mathbf{A}]^{-1} \mathbf{A}^T \mathbf{c}$ (Equation 6). The initial value for the predicted data
¹⁸⁴ should be close to the observed data. We found that in practice a reasonably fast convergence
¹⁸⁵ is achieved by assigning $\mathbf{d}_0 = 0.9 \mathbf{d}^o$.

¹⁸⁶ Convergence of the solution cannot be directly evaluated by the value of the Lagrangian
¹⁸⁷ (Equation 12) because values $\boldsymbol{\lambda}$ are not calculated. Instead, we specify a *merit function* \mathcal{M}
¹⁸⁸ which combines the data misfit as well as the adherence to the constraints

$$\mathcal{M}_k(\mathbf{p}_k, \mathbf{d}_k) = \sqrt{\mathbf{r}_k^T \mathbf{W} \mathbf{r}_k} + \nu \sqrt{\mathbf{e}_k^T \mathbf{e}_k} . \quad (28)$$

¹⁸⁹ in which $\sqrt{\mathbf{r}_k^T \mathbf{W} \mathbf{r}_k}$ is the *weighted root-mean-squared error* (WRMSE) and ν is a trade-off
¹⁹⁰ parameter that balances fitting the data and strict adherence to the constraints. In practice, we
¹⁹¹ have found that a value of $\nu = 0.1$ works well in all of our synthetic data tests and our field data
¹⁹² application. The merit function is evaluated at every iteration. The non-linear optimisation
¹⁹³ stops when a given maximum number of iterations is reached, the merit function increases, or
¹⁹⁴ when the change in its value drops below a given threshold.

¹⁹⁵ An outline of the entire Euler inversion procedure is given in Algorithm 1. Notice that
¹⁹⁶ Equations 24 and 26 for calculating $\Delta\mathbf{p}_k$ and $\Delta\mathbf{d}_k$ do not depend on $\boldsymbol{\lambda}_k$ or $\Delta\boldsymbol{\lambda}_k$. Thus,
¹⁹⁷ Equation 25 does not need to be calculated in practice.

¹⁹⁸ **2.3.2 Structural index estimation**

¹⁹⁹ An advantage of Euler inversion over Euler deconvolution is its ability to obtain predicted
²⁰⁰ values of the potential field and its gradient. In Section 3.2, we demonstrate that the *weighted*

Algorithm 1: The Euler inversion Gauss-Newton optimization method.

```
1 Set  $\mathbf{p}_0 = [\mathbf{A}^T \mathbf{A}]^{-1} \mathbf{A}^T \mathbf{c}$  and  $\mathbf{d}_0 = 0.9 \mathbf{d}^o$  ;
2 Evaluate  $\mathcal{M}_0(\mathbf{p}_0, \mathbf{d}_0)$  ;
3 for  $k = 0$  to  $L - 1$  do
4   Calculate the parameter correction  $\Delta\mathbf{p}_k$  using Equation 24 ;
5   Calculate the predicted data correction  $\Delta\mathbf{d}_k$  using Equation 26 ;
6   Update  $\mathbf{p}_{k+1} = \mathbf{p}_k + \Delta\mathbf{p}_k$  and  $\mathbf{d}_{k+1} = \mathbf{d}_k + \Delta\mathbf{d}_k$  ;
7   Evaluate  $\mathcal{M}_{k+1}(\mathbf{p}_{k+1}, \mathbf{d}_{k+1})$  ;
8   if  $\mathcal{M}_{k+1} > \mathcal{M}_k$  then
9     Undo the previous update of  $\mathbf{p}$  and  $\mathbf{d}$  ;
10    Exit ;
11   end if
12   if  $|\mathcal{M}_{k+1} - \mathcal{M}_k| / \mathcal{M}_k < \delta$  then
13     Exit ;
14   end if
15 end for
16 Calculate the  $\hat{\sigma}_0^2$  using the last residuals  $\mathbf{r}_L$  ;
17 Calculate  $\mathbf{C}_p$  using Equation 27 ;
```

201 *root-mean-squared error*

$$\text{WRMSE} = \sqrt{[\mathbf{d}^o - \mathbf{d}_L]^T \mathbf{W} [\mathbf{d}^o - \mathbf{d}_L]}, \quad (29)$$

202 of the predicted data at the L -th iteration \mathbf{d}_L appears to be smallest when the correct structural
203 index η is used. Given this observation, we can estimate the optimal value of η by running the
204 Euler inversion in a given data window for different values of η and choosing the one that
205 produces the smallest WRMSE. This procedure is summarised in Algorithm 2.

Algorithm 2: Structural index estimation through Euler inversion.

```
1 for  $\eta = \eta_{min}$  to  $\eta_{max}$  do
2   Run Algorithm 1 to estimate  $\mathbf{p}_\eta$  and  $\mathbf{d}_\eta$  ;
3   Calculate the WRMSE( $\eta$ ) =  $\sqrt{[\mathbf{d}^o - \mathbf{d}_\eta]^T \mathbf{W} [\mathbf{d}^o - \mathbf{d}_\eta]}$  for the estimated  $\mathbf{d}_\eta$  ;
4 end for
5 Choose optimal  $\eta = \operatorname{argmin}_\eta \text{WRMSE}(\eta)$  and the corresponding  $\mathbf{p}_\eta$  and  $\mathbf{d}_\eta$  ;
```

206 **2.3.3 Moving window procedure**

207 For cases with multiple sources in a given dataset, we adopt a moving window procedure similar
208 to the classic Euler deconvolution. We divide the data region into M overlapping windows. For
209 each window, we run Algorithm 2 to obtain an estimate of the parameters and the structural
210 index η . This procedure leads to spurious solutions, much like standard Euler deconvolution,
211 in cases where there are no sources inside windows or when sources are heavily truncated. To
212 filter out spurious sources, we rank the solutions for each structural index separately by the
213 variance of the z_o estimate (from Equation 27) and keep only a given percentage of those with
214 the smallest variance. This procedure is summarised in Algorithm 3.

Algorithm 3: Moving window procedure for Euler inversion.

```
1 Divide the data region into  $M$  overlapping windows with a defined degree of overlap ;
2 Define a ratio  $0 < \gamma \leq 1$  of estimates to keep ;
3 for  $l = 1$  to  $M$  do
4   Run Algorithm 2 on the data from window  $l$  to estimate  $\mathbf{p}$ ,  $\mathbf{d}$ ,  $\mathbf{C}_p$ , and  $\eta$  ;
5 end for
6 for  $\eta = \eta_{min}$  to  $\eta_{max}$  do
7   Sort the  $M_\eta$  solutions which produced an estimated SI equal to  $\eta$  by the estimated
     variance of  $z_o$  in increasing order ;
8   Keep the first  $\gamma M_\eta$  solutions and discard the remainder ;
9 end for
```

215

3 Results

216 In this section, we demonstrate the effectiveness and limitations of the Euler inversion method
217 by applying it to a series of synthetic datasets and to real aeromagnetic data from Rio de Janeiro,
218 Brazil. The applications are organised as follows:

- 219 1. **Method demonstration:** This test uses a single data window and a single dipolar source.
220 Its aim is to demonstrate the convergence of the Euler inversion method and its ability
221 to correctly estimate the source position when the structural index is known, even in the
222 presence of random noise.
- 223 2. **Effect of structural index choice:** This test uses several different sources, each in a
224 separate data window, and runs the Euler inversion method on each with different values
225 of the structural index η . Its aim is to determine the effect of the choice of η on the
226 estimated coordinates and the weighted root-mean-squared error (Equation 28).
- 227 3. **Effect of random noise:** This test uses a single dipolar source and a single data window
228 with data contaminated with increasing levels of pseudo-random noise. Its aim is to
229 investigate the effect of random high-frequency noise on the Euler inversion estimated
230 source coordinates, base level, and structural index.
- 231 4. **Effect of interfering sources:** This test uses four different models of a dipolar source
232 and a single data window with an interfering dipolar source present in different locations
233 and depths. Its aim is to investigate the effect of interfering sources inside the data window
234 on the Euler inversion, Euler deconvolution, and finite-difference Euler deconvolution
235 results.
- 236 5. **Moving window procedure with multiple sources:** This test combines several
237 sources and uses the moving window procedure from Algorithm 3. Its aim is to show
238 how the Euler inversion method behaves on a more complex dataset and provide a com-
239 parison with standard Euler deconvolution and finite-difference Euler deconvolution.

240 6. **Aeromagnetic data from Rio de Janeiro, Brazil:** This test applies the Euler inver-
241 sion method to a real dataset which contains multiple sources. Its aim is to demonstrate
242 the effectiveness of the method on a real dataset with realistic levels of noise, signal overlap,
243 and geometry of sources.

244 The Python source code used to produce the results presented here, as well as extra explanation
245 of the models and procedures, can be found in the supplementary information at <https://doi.org/10.6084/m9.figshare.26384140> (Uieda et al., 2024).

247 3.1 Method demonstration

248 The main goal of this synthetic data test is to demonstrate the general effectiveness of the Euler
249 inversion method to estimate the position and base level of a single source. To this end, we cre-
250 ated a model composed of a single dipole located at ($x_o = 15\,000\text{ m}$, $y_o = 12\,000\text{ m}$, $z_o = -3000\text{ m}$)
251 with a dipole moment magnitude of $5 \times 10^{11}\text{ A m}^{-1}$, inclination of -30° , and declination of 15° .
252 The reference field direction was the same as the dipole moment direction. The synthetic total-
253 field magnetic anomaly data was calculated on a regular grid with point spacing of 300 m at a
254 height of 800 m. To the data, we added a base level of 100 nT and pseudo-random Gaussian
255 noise with 0 nT mean and 10 nT standard deviation. The eastward and northward derivatives
256 of the total-field anomaly grid were calculated with a central-difference scheme. The upward
257 derivative was calculated by Fast Fourier Transform (FFT). The synthetic anomaly and its three
258 derivatives are shown in Figures 1a-d.

259 The Euler inversion method described in Algorithm 1 was applied to the synthetic data.
260 We chose a fixed structural index of $\eta = 3$, which is the correct index for a magnetic dipole.
261 For data weights, we used 1 for the total-field anomaly, 0.1 for the east-derivative, 0.1 for the
262 north-derivative, and 0.025 for the upward-derivative. These weights were chosen to counteract
263 the increased effect of noise on the derivatives, particularly the upward derivative which was cal-
264 culated through FFT. Figures 1e-h show the inversion residuals after convergence was achieved
265 ($L = 6$ iterations) for the total-field anomaly and its eastward, northward, and upward deriva-
266 tives, respectively. Also shown are the true source location, the initial source location (the Euler

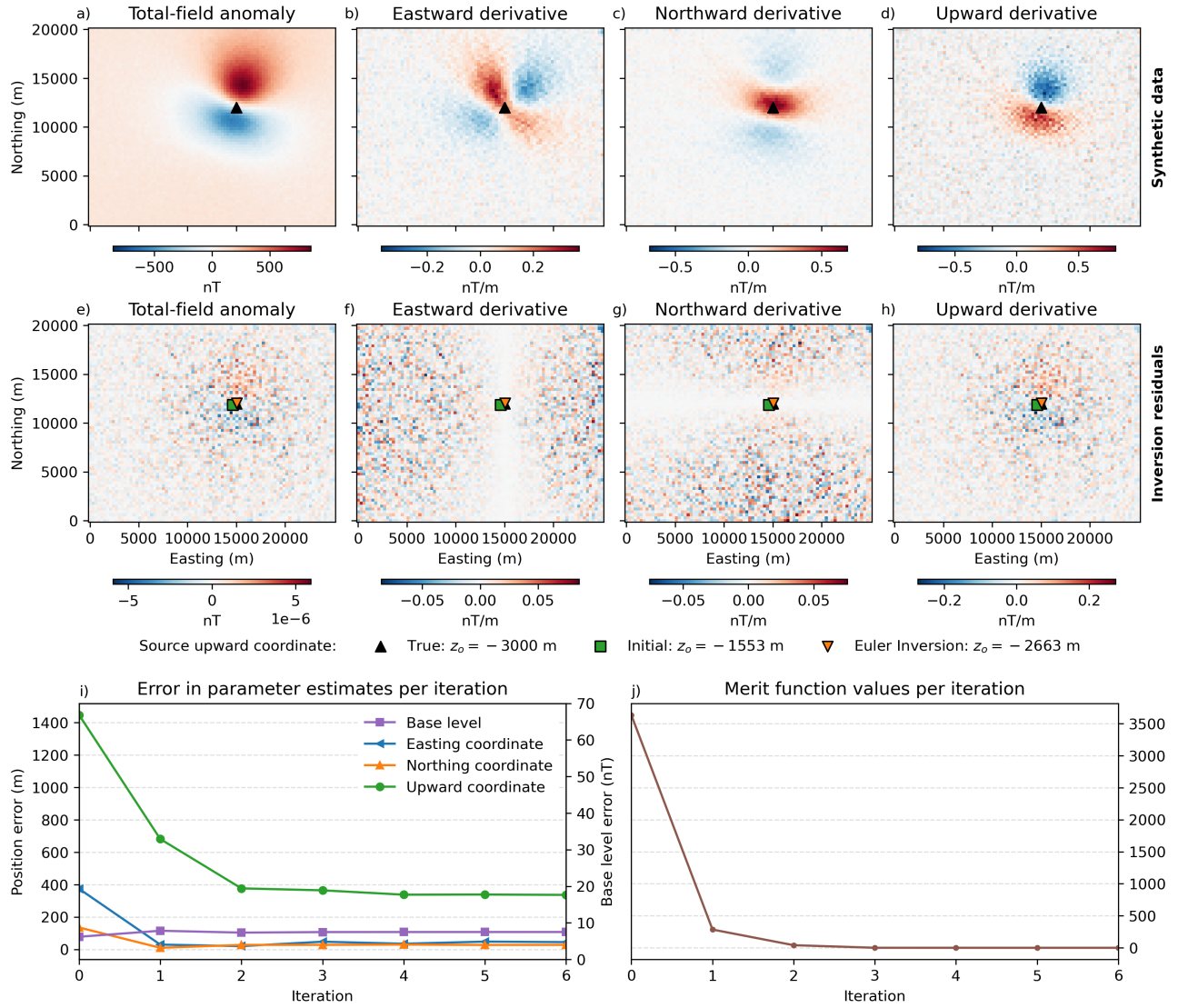


Figure 1: Data and results from the synthetic data test to demonstrate the performance of the method on a single target. a-d) The noise-corrupted synthetic total-field anomaly and its eastward, northward, and upward derivatives, respectively. The position of the dipolar source is marked by the black triangle. e-h) The Euler inversion residuals (observed data minus predicted data) for the total-field anomaly and its easting, northing, and upward derivatives, respectively. The black triangle shows the true location of the source, the green square shows the location estimated by Euler deconvolution, and the orange triangle shows the location estimated by Euler inversion. i) The error in the estimate of the easting (blue line), northing (orange line), and upward (green line) coordinates of the source and the base level (purple line) as a function of the Gauss-Newton iteration (Algorithm 1). j) The value of the merit function \mathcal{M} (Equation 28) per Gauss-Newton iteration.

267 deconvolution result), and the predicted source location from Euler inversion. The final Euler
 268 inversion prediction of the source location was ($x_o = 15\,045$ m, $y_o = 12\,028$ m, $z_o = -2663$ m)
 269 and the estimated base level was $b = 93$ nT, which is an improvement on the estimated values

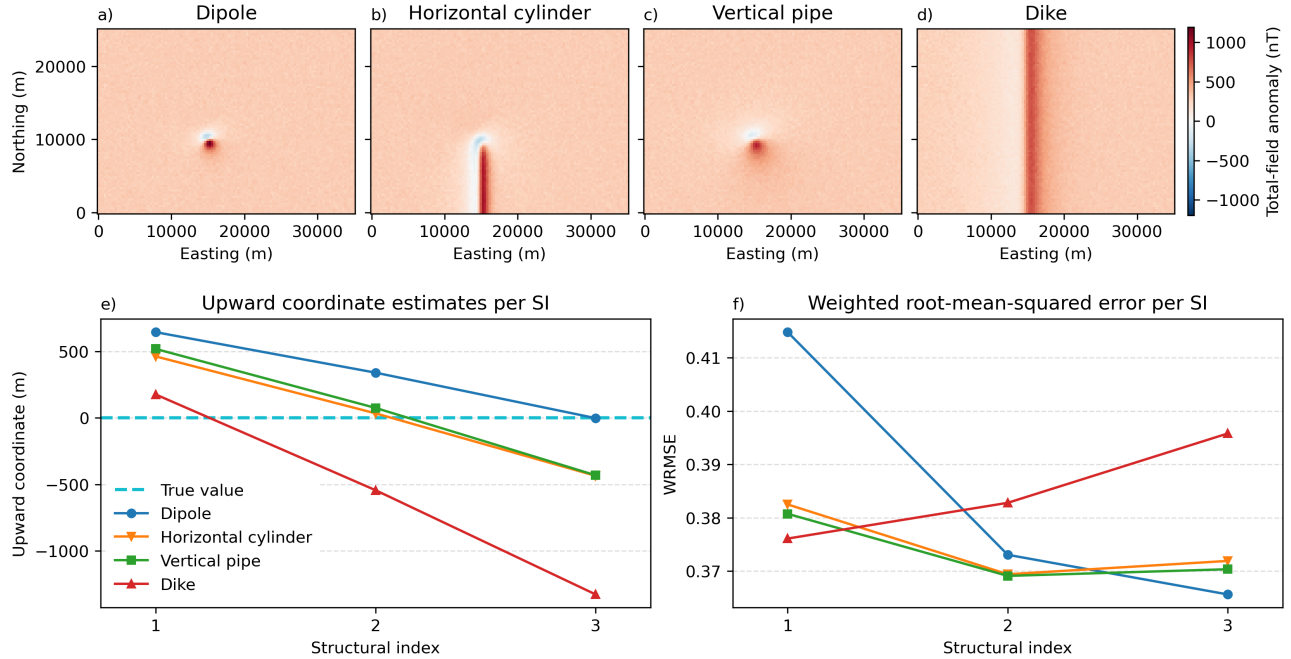


Figure 2: Data and results from the synthetic data test using different values of structural index η for different source types. a-d) Noise-corrupted total-field magnetic anomaly data caused by a dipole ($\eta = 3$), a horizontal cylinder ($\eta = 2$), a vertical pipe ($\eta = 2$), and a vertical North-South dyke ($\eta = 1$), respectively. e) Estimate of the upward source coordinate z_o as a function of structural index for the dipole (blue line), horizontal cylinder (orange line), vertical pipe (green line), and dyke (red line). The true upward coordinate of the sources ($z_o = 0$ m) is marked by the blue dashed line. Note that the z_o estimate is closest to the true value when the correct structural index for each source type is used. f) The weighted root-mean-squared error (WRMSE; Equation 29) as a function of structural index for the dipole (blue line), horizontal cylinder (orange line), vertical pipe (green line), and dyke (red line). The WRMSE is minimum for each source type when the correct structural index is used.

270 by Euler deconvolution (Figure 1).

271 The convergence of the solution is shown in Figures 1i-j. The error in the estimated source
 272 coordinates and base level are shown in Figure 1i. The error in the x_o (easting) and y_o (northing)
 273 coordinates, as well as the base level, do not vary greatly from the initial solution. However, the
 274 error in the z_o (upward) coordinate drops from over 1400 m to less than 400 m in two iterations.
 275 The merit function (Equation 28) also drops sharply in value by two iterations, as can be seen
 276 in Figure 1j, confirming the rapid convergence of the Euler inversion method.

277 **3.2 Effect of structural index choice**

278 In this synthetic data test, we created datasets using four different models: a dipole, a hori-
279 zontal cylinder composed of a right-rectangular prism stretched in the southward direction, a
280 vertical pipe composed of a right-rectangular prism stretched in the downward direction, and
281 a vertical dyke composed of a right-rectangular prism stretched in the southward, northward,
282 and downward directions. All models share the same true location of ($x_o = 15\,000\text{ m}$, $y_o =$
283 $10\,000\text{ m}$, $z_o = 0\text{ m}$), base level of 300 nT , and induced magnetisation with inclination of 35° and
284 declination of -20° . The data were generated on a regular grid with spacing of 300 m , height
285 of 1000 m , and contaminated with pseudo-random Gaussian noise with 0 nT mean and 15 nT
286 standard deviation. Figures 2a-d show the synthetic noise-corrupted total-field anomaly data.

287 We ran the Euler inversion method on each data grid three times, each time changing
288 the structural index between one, two, and three. Figure 2e shows the upward coordinate z_o
289 estimated for each of the four models as a function of the structural index η . The Euler inversion
290 estimated z_o correlates with η , with larger values of the structural index leading to deeper source
291 estimates. Values closest to the true $z_o = 0\text{ m}$ are achieved when the correct structural index is
292 used ($\eta = 1$ for the dyke, $\eta = 2$ for the cylinder and pipe, and $\eta = 3$ for the dipole). Figure 2f
293 shows the weighted root-mean-squared error (WRMSE; Equation 29) at the final iteration of
294 the Euler inversion method for all four models as a function of structural index. The WRMSE is
295 a measure of goodness-of-fit between the predicted total-field anomaly and its three derivatives
296 and their observed counterparts. The WRMSE is minimum for all four models when the correct
297 structural index is used.

298 **3.3 Effect of random noise**

299 We conducted another experiment to determine the effect of random high-frequency noise on
300 the Euler inversion estimates. To this end, we created synthetic data from a dipole model
301 located at ($x_o = 15\,000\text{ m}$, $y_o = 11\,000\text{ m}$, $z_o = -5000\text{ m}$) and with a dipole moment magnitude
302 of $2 \times 10^{12}\text{ A m}^{-1}$, inclination of -30° , and declination of 15° . The total-field anomaly data

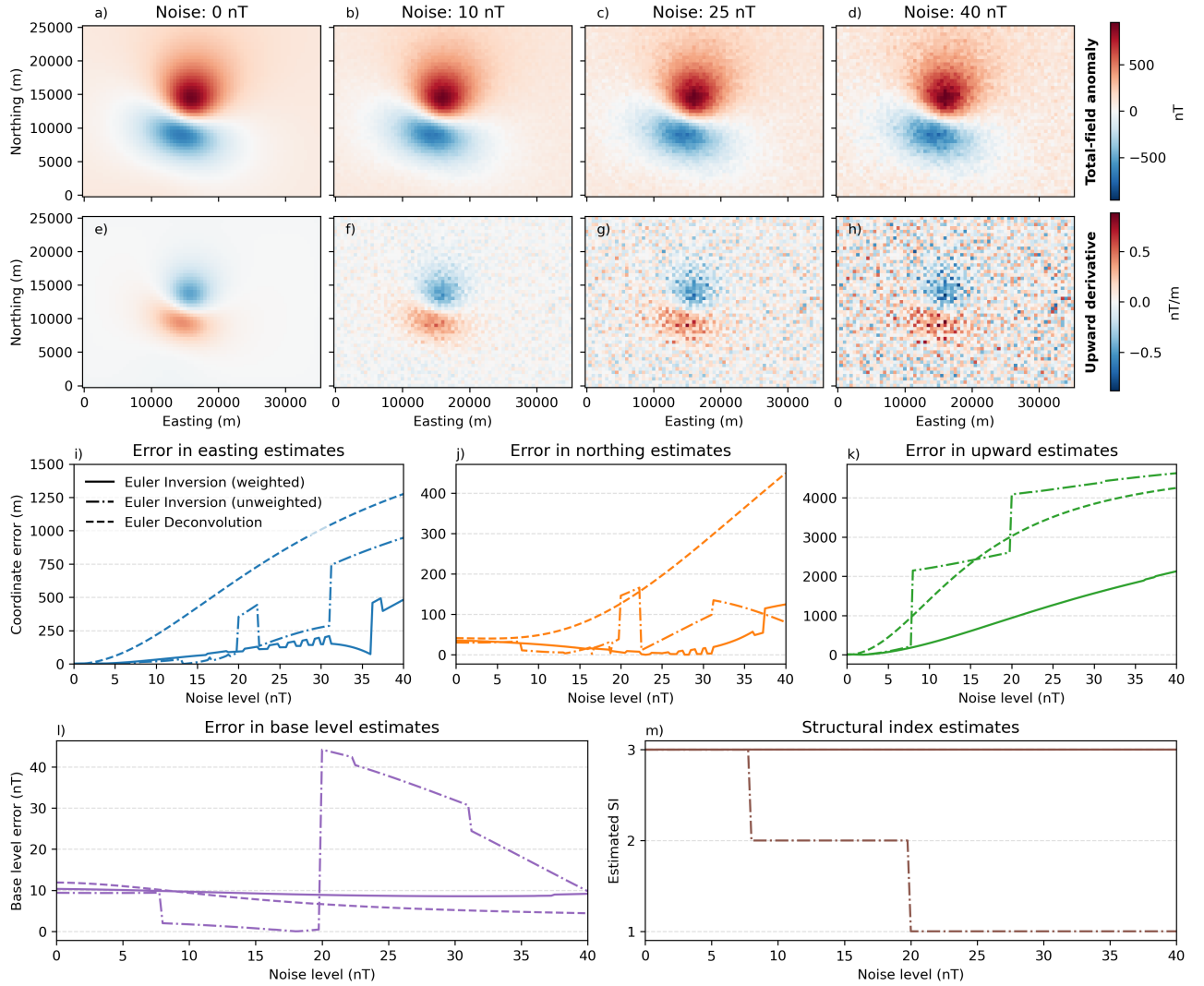


Figure 3: Data and results from the synthetic data test used to investigate the effect of high-frequency noise on the Euler inversion results. a-d) Noise-corrupted total-field magnetic anomaly of a dipolar source for noise levels 0, 10, 25, and 40 nT. e-h) The upward derivative of the data in a-d, calculated by FFT. i-k) Error in the estimated easting, northing, and upward coordinates, respectively. l) Error in the estimated base level. m) The estimated structural index η using Algorithm 2. The lines in i-m are the results for Euler deconvolution (dashed line), Euler inversion without data weights (dashed-dotted line), and Euler inversion with weights (solid line) 1 for the total-field anomaly, 0.1 for the eastward derivative, 0.1 for the northward derivative, and 0.025 for the upward derivative.

were generated on a regular grid with a spacing of 500 m and a constant height of 800 m. The reference field direction was the same as the dipole moment direction. A base level of 100 nT was added to the data. We generated different datasets by adding pseudo-random Gaussian noise with 0 nT mean and standard deviations varying from 0 nT to 40 nT with a step of 0.2 nT. Figures 3a-d show the synthetic data for noise levels 0, 10, 25, and 40 nT, while Figures 3e-h

308 show the upward derivative calculated from the total-field anomaly through FFT.

309 On each dataset, we ran Euler deconvolution (Equation 6), Euler inversion with unit weights,
310 and Euler inversion with weights 1 for the total-field anomaly, 0.1 for the eastward derivative,
311 0.1 for the northward derivative, and 0.025 for the upward derivative. Both Euler inversion
312 runs used the structural index estimation procedure (Algorithm 2). Figures 2i-1 show the error
313 in the estimated easting, northing, and upward coordinates as well as the base level for each
314 of the methods as a function of noise level. The error in each of three coordinates raises
315 sharply with noise level for Euler deconvolution, particularly for the upward z_o coordinate.
316 The unweighted Euler inversion results vary less regularly but the present errors are just as
317 large as Euler deconvolution for the upward coordinate. However, the weighted Euler inversion
318 presented overall smaller errors and a slower growth curve for the upward coordinate error than
319 the other two methods. The base level error is nearly constant at approximately 10 nT for
320 Euler deconvolution and the weighted Euler inversion, but varies to as much as 40 nT for the
321 unweighted Euler inversion.

322 Figure 3m shows the estimated structural index η for the weighted and unweighted Euler
323 inversion as a function of noise level. The unweighted Euler inversion estimated the wrong
324 structural index $\eta = 2$ from approximately noise level 7 nT and $\eta = 1$ from approximately noise
325 level 20 nT. These jumps in the estimated structural index appear to correlate with jumps in
326 the base level and z_o coordinate errors. The weighted Euler inversion was able to estimate the
327 correct structural index ($\eta = 3$) for all noise levels tested.

328 3.4 Effect of interfering sources

329 Another common issue encountered during the application of Euler-based methods is the pres-
330 ence of interfering sources within the data window. To test this effect on Euler inversion, we
331 create four different synthetic total-field anomaly datasets. All contain a main dipole located at
332 ($x_o = 13\,000$ m, $y_o = 11\,000$ m, $z_o = -4000$ m) with a dipole moment amplitude of 1×10^{12} A m⁻¹,
333 inclination of -30° , and declination of 15° . The reference field direction was the same as the
334 dipole moment direction. Each of the four models also contain a second dipolar source, simu-

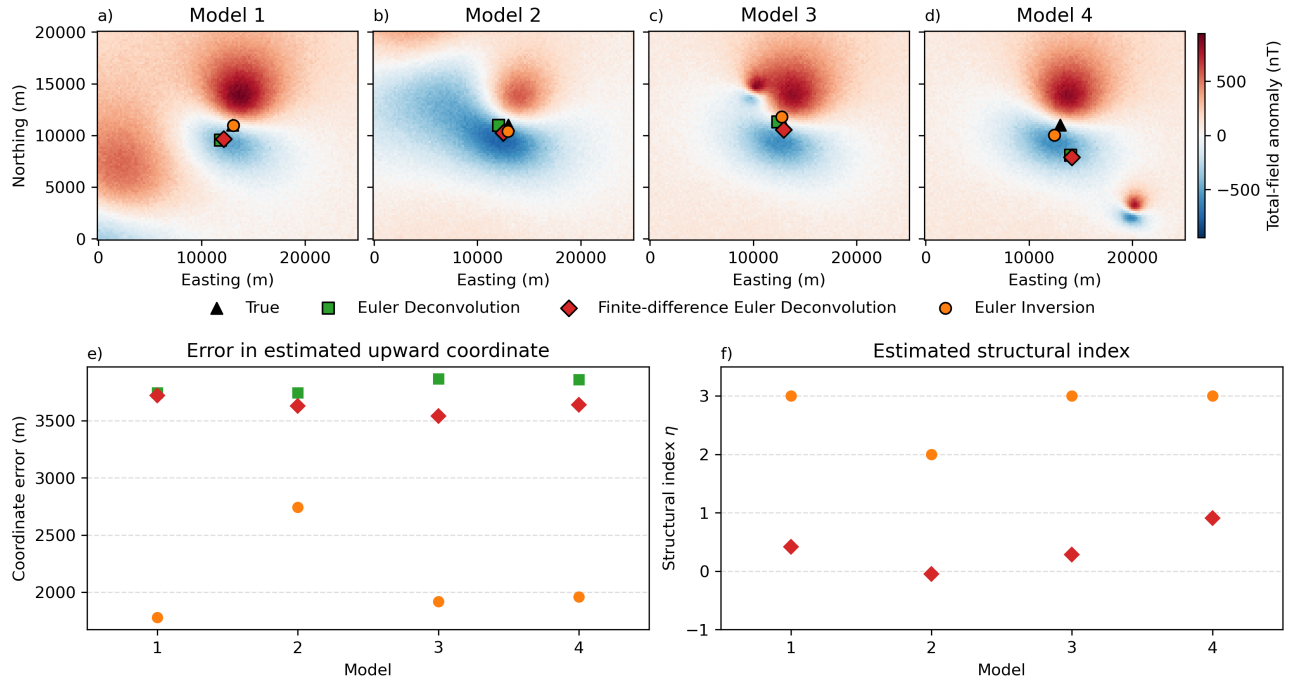


Figure 4: Data and results from the synthetic data test used to investigate the effect of interfering sources inside the data window on the Euler inversion results. a-d) Noise-corrupted total-field magnetic anomaly for four models, each of which include the same central dipole but different interfering sources in the form of another dipolar source. Also plotted are the estimated positions from Euler deconvolution, finite-difference Euler deconvolution, and Euler inversion. e) The error in the estimated upward coordinate of the source z_o for each of the Euler methods as a function of the model number. f) The estimated structural index η for Euler inversion and finite-difference Euler deconvolution as a function of the model number. The true source location is represented by a black triangle, the Euler deconvolution result by a green square, the finite-difference Euler deconvolution result by a red diamond, and the Euler inversion result by an orange circle.

lating an interfering source in the data window, that is located at different places and depths relative to the main dipole. The total-field anomaly data were generated on regular grids with a spacing of 200 m and at a constant height of 800 m. We added to all datasets a base level of 100 nT and pseudo-random Gaussian noise with 0 nT mean and 20 nT standard deviation. Figures 4a-d show the noise-corrupted total-field anomaly for each of the models.

On each dataset we, ran Euler deconvolution (Equation 6 with structural index $\eta = 3$), the finite-difference Euler deconvolution method of Gerovska et al. (2005), and Euler inversion with the structural index estimation (Algorithm 2) and data weights of 1 for the total-field anomaly, 0.1 for the eastward derivative, 0.1 for the northward derivative, and 0.025 for the upward

derivative. The estimated easting and northing coordinates are shown in Figures 4a-d. For models 2 and 3, all three methods performed similarly in estimating the horizontal coordinates of the true source. For models 1 and 4, the Euler deconvolution and finite-difference Euler deconvolution results are comparable, whilst the Euler inversion results are closer to the true source location. Figure 4e shows the error in the estimated upward coordinate for all three methods and four models. The Euler inversion errors are consistently lower than those of both Euler deconvolution methods. With the exception of model 2, the Euler inversion error on the upward coordinate are approximately half those of the Euler deconvolution methods. Figure 4f shows the estimated structural index for finite-difference Euler deconvolution and Euler inversion. The finite-difference Euler deconvolution method consistently estimated values lower than $\eta = 1$. With the exception of model 2, Euler inversion was able to estimate the correct structural index ($\eta = 3$) for all other models.

3.5 Moving window procedure with multiple sources

To simulate a more realistic dataset, we created a model composed of 10 sources combining dipoles at various locations and depths and vertical dykes at various orientations. All sources had induced magnetisation in the direction of the regional field with a inclination of -30° and declination of -20° . The total-field anomaly of the model was calculated on a regular grid with a spacing of 500 m and at a constant height of 1000 m. We added to the data a base level of 1000 nT, pseudo-random Gaussian noise with 0 nT and 50 nT standard deviation, and a regional field composed of a first-degree polynomial with angular coefficients of 0.02 nT m^{-1} in the eastward and -0.03 nT m^{-1} in the northward directions. The noise-corrupted total-field anomaly data are shown in Figure 5a.

To the dataset, we applied the moving window Euler inversion method (Algorithm 3), the finite-difference Euler deconvolution method of Gerovska et al. (2005), and standard Euler deconvolution (using structural indices 1, 2, and 3). Euler inversion was performed with data weights of 1 for the total-field anomaly, 0.1 for the eastward derivative, 0.1 for the northward derivative, and 0.025 for the upward derivative. All three methods used the same moving

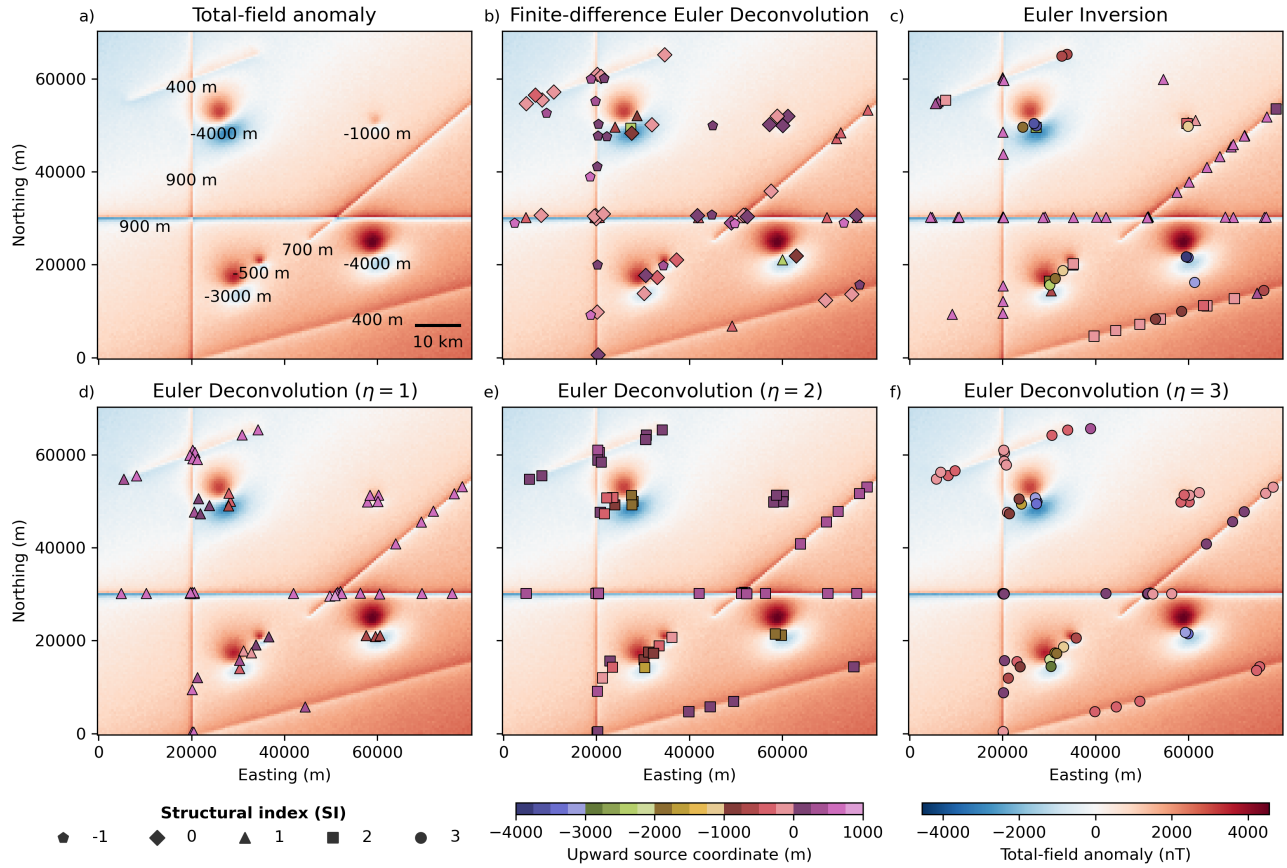


Figure 5: Data and results from the synthetic data test using the moving window scheme (Algorithm 3). a) Noise-corrupted total-field magnetic anomaly generated from 10 sources with overlapping signals, including dykes and dipoles. The true upward coordinate z_o of each source is shown next to their respective anomalies. b-f) The estimated source locations from finite-difference Euler deconvolution, Euler inversion, Euler deconvolution ($\eta = 1$), Euler deconvolution ($\eta = 2$), and Euler deconvolution ($\eta = 3$), respectively. The total-field anomaly is shown in the background for reference. The structural index of the solutions are represented by pentagons ($\eta = -1$), diamonds ($\eta = 0$), triangles ($\eta = 1$), squares ($\eta = 2$), and circles ($\eta = 3$). For finite-difference Euler deconvolution (b), the structural index symbol is that of the closest integer to the estimated value. The color of each symbol represents the estimated upward coordinate z_o . The window size used was 10 000 m and the step between windows was 5000 m.

371 window procedure described in Algorithm 3 for the sake of comparison. The windows had a size
 372 of 10 000 m and were moved by 5000 m at a time. The ratio of estimates kept to form the final
 373 solution was $\gamma = 0.3$ for Euler deconvolution, $\gamma = 0.35$ for finite-difference Euler deconvolution,
 374 and $\gamma = 0.25$ for Euler inversion.

375 Figures 5b-f show the estimated source positions and structural indices for finite-difference
 376 Euler deconvolution, Euler inversion, and Euler deconvolution with structural indices 1, 2, and

377 3, respectively. The finite-difference method estimates a non-integer structural index, as a result
378 Figure 5b shows the closest integer value to the actual estimated η . The finite-difference Euler
379 deconvolution method underestimates the structural indices of all sources and, therefore, also
380 underestimates their depths. The finite-difference method solutions are also more scattered than
381 their Euler deconvolution and Euler inversion counterparts. The Euler deconvolution results
382 are closer to the correct depths when the correct structural index is used. They present larger
383 dispersion than Euler inversion in areas where the signals of multiple sources overlap. With
384 the exception of the deeper dykes in the northwest and southeast and the small dipole with
385 $z_o = -500$ m, Euler inversion is able to estimate the correct structural index for most sources.
386 The upward coordinate estimates for Euler inversion are also closer than Euler deconvolution
387 to their true values when the correct structural index was estimated. Euler inversion notably
388 estimates an incorrect η and z_o for smaller sources when there is a large amount of interference
389 in the anomalies and for dykes that are deeper and produce a smoother signal.

390 3.6 Aeromagnetic data from Rio de Janeiro

391 The geology of Rio de Janeiro state (Southeastern Brazil) consists primarily of high-grade meta-
392 morphic rocks and granitoid magmatism related to the Ribeira Belt (RB) ([Heilbron et al., 2020](#)).
393 Figure 6a shows a simplified geologic map of the area, which was modified from [Heilbron et al.](#)
394 ([2016](#)) and [Dantas et al. \(2017\)](#). The Ribeira Belt is traditionally interpreted as a thrust belt
395 formed by diachronous collisions mainly between the São Francisco and Congo paleocontinents
396 ([Heilbron et al., 2008; Trouw et al., 2000](#)) or by an intracontinental orogeny (e.g. [Meira et al.,](#)
397 [2019, 2015](#)), during the Brasiliano orogeny. This process culminated in an orogen-parallel, steep
398 strike-slip shear system ([Egydio-Silva et al., 2005](#)), which deformed the Paleoproterozoic base-
399 ment rocks and reworked the Meso- to Neoproterozoic metasedimentary units (for example, the
400 Italva and São Fidelis groups) and syn-orogenic granitoid plutons (for example, the Rio Ne-
401 gro complex) which formed during the orogeny ([Heilbron and Machado, 2003; Heilbron et al.,](#)
402 [2020](#)). These tectonic events imprinted a distinct NE-ENE-trending structural pattern onto
403 these rocks.

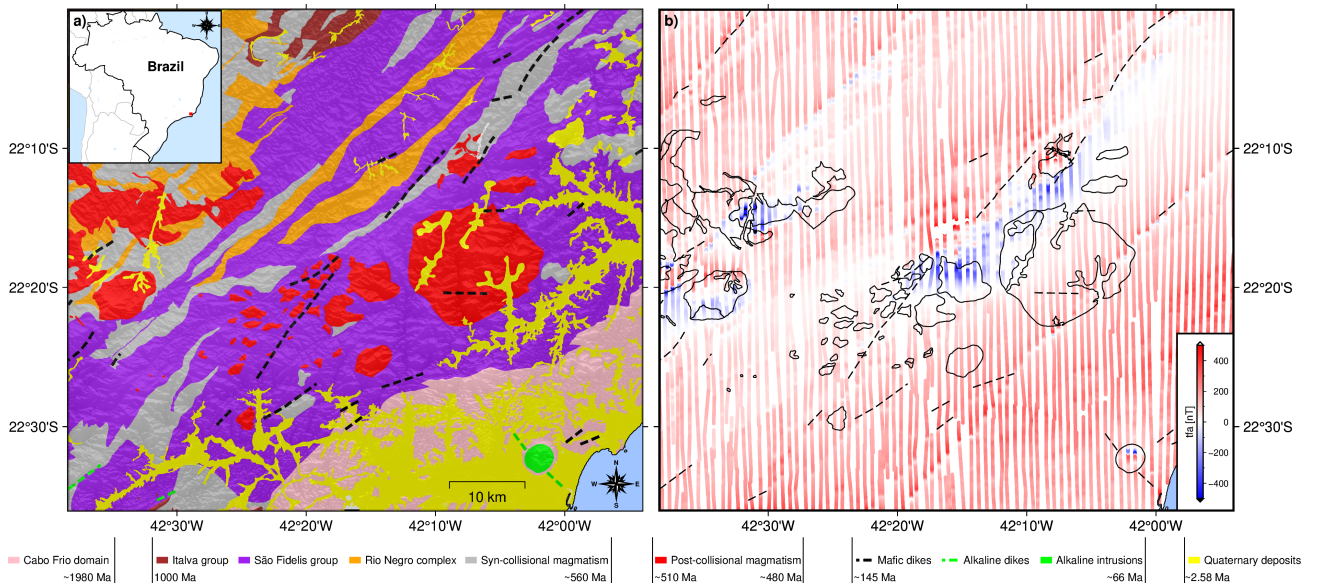


Figure 6: Geologic map and observed total-field magnetic anomaly data from the west of the state of Rio de Janeiro, Brazil. a) Simplified geologic map showing the main groups and dykes that outcrop in the region. In pink is the Cabo Frio domain, dark red is the Italva group, purple is the São Fidelis group, orange is the Rio Negro complex, gray is the syn-collisional magmatism, red is the post-collisional magmatism, green are alkaline intrusions, yellow are the Quaternary deposits, and the dashed lines are mafic and alkaline dykes. b) The aeromagnetic flight-line data, overlaid by the outlines of the post-collisional magmatism and alkaline intrusions (solid black lines) and dykes (dashed lines). The geologic map was modified from Heilbron et al. (2016) and Dantas et al. (2017).

The late Neoproterozoic to Cambrian period witnessed post-orogenic magmatism (*e.g.*, Valeriano et al., 2011), marking the final stages of the West Gondwana amalgamation. After this, the region remained tectonically quiescent until the Lower Cretaceous, when reactivation occurred with the emplacement of the NE-trending Serra do Mar mafic dyke swarm, preceding the break-up of West Gondwana and the opening of the South Atlantic Ocean (Almeida et al., 2013). Lastly, thermal anomalies in the region during the Upper Cretaceous to Paleocene period led to the emplacement of alkaline complexes and dykes (Thompson et al., 1998). The geological complexity of the Ribeira Belt, marked by the interplay of diverse tectonic regimes and magmatic events (Figure 6a), makes the Rio de Janeiro region an ideal test case for Euler inversion.

We used aeromagnetic data from the state of Rio de Janeiro which are distributed by the Serviço Geológico do Brasil (<https://geosgb.sgb.gov.br>). The data were collected in two phases:

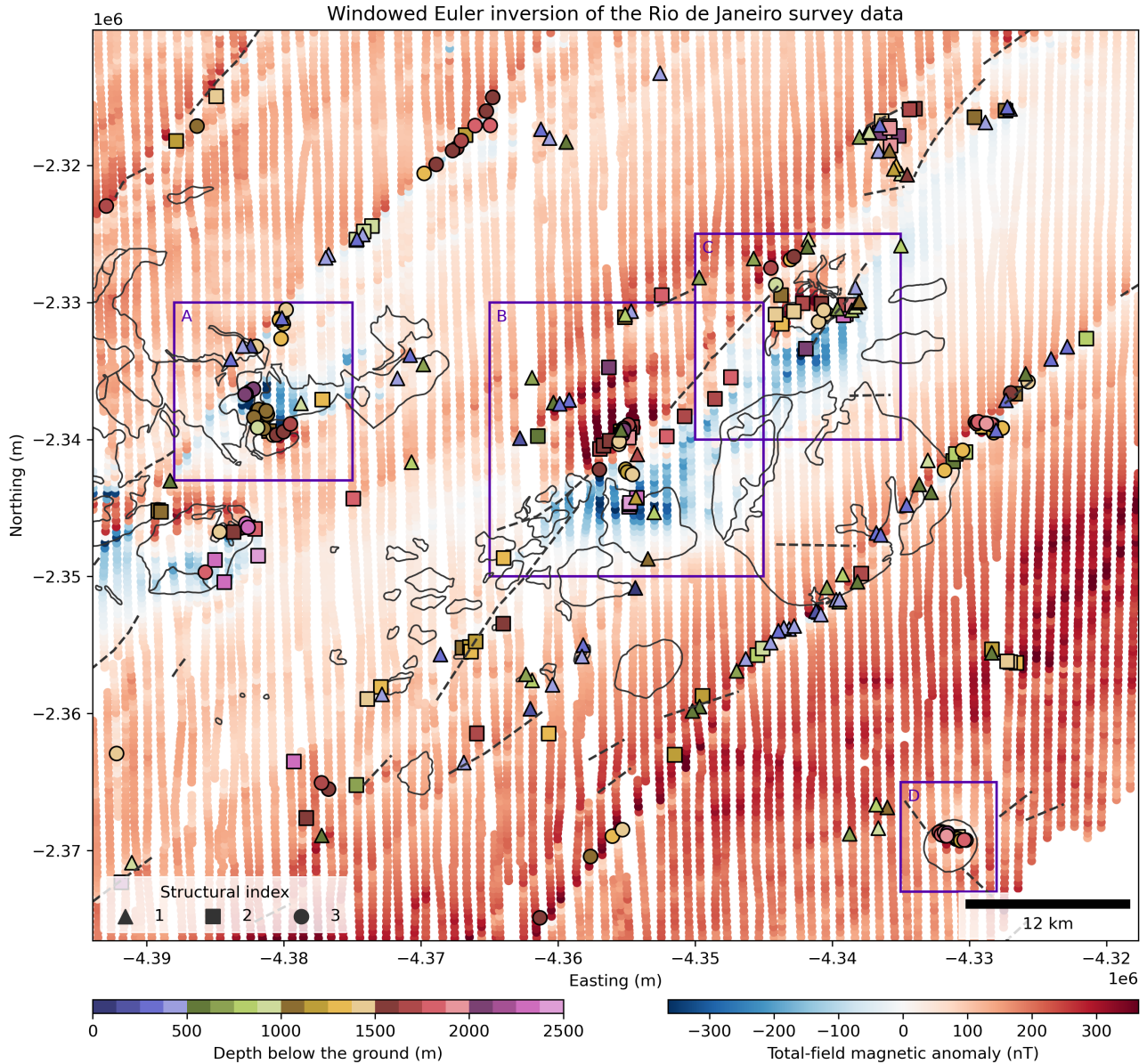


Figure 7: Results of applying Euler inversion with a window size of 12 000 m and a window step of 2400 m to the aeromagnetic data from Rio de Janeiro, Brazil. Estimated source locations and structural indices obtained from Euler inversion are shown as triangles ($\eta = 1$), squares ($\eta = 2$), and circles ($\eta = 3$). The colour of each symbol represents the estimated depth below the surface of the Earth (topography). Also shown are the total-field anomaly flight-line data, the contours of the post-collisional magmatism and alkaline intrusions (solid black lines) and dykes (dashed lines). The purple squares highlight the A, B, C, and D anomalies that are discussed in the text.

Subarea 1 was surveyed between March 25 and May 27, 1978, using an Islander aircraft (PT-KRP), while Subarea 2 was surveyed between April 6 and July 19, 1978, using a Bandeirante aircraft (PT-GKJ), both funded by the Brazilian government. As shown in Figure 6b, the survey

419 followed a pattern of north-south flight lines spaced approximately 1 km apart, with east-west
420 tie lines. Data were recorded at 100-meter intervals using a Geometrics G-803 magnetometer.
421 Some of the notable features of the data are the NE-SW linear features (interpreted here as
422 dykes), which coincide with known dyke outcrops, and complex dipolar anomalies which coincide
423 with some of the post-collisional magmatism and alkaline intrusions. A subset of 50 882 data
424 points were used in our analysis.

425 The data were not interpolated on a regular grid to avoid any smoothing effects that the
426 interpolation might have on the linear features. This could result in an over-estimation of their
427 depth, as discussed in Section 3.5. Instead, we used the gradient-boosted equivalent sources
428 method of Soler and Uieda (2021) to fit a model to the observed line data. We then used
429 the model to make predictions of the three spatial derivatives at the original measurement
430 locations by a central-difference method with a coordinate shift of 1 m. Further details about
431 the data processing can be found in the source code archive that accompanies this article
432 <https://doi.org/10.6084/m9.figshare.26384140> (Uieda et al., 2024).

433 We performed the moving-window Euler inversion (Algorithm 3) on the observed total-field
434 anomaly line data using windows of size of 12 000 m which were moved 2400 m at a time. The
435 proportion of solutions kept was $\gamma = 0.15$. The inversion was performed with data weights of
436 1 for the total-field anomaly, 0.1 for the eastward derivative, 0.1 for the northward derivative,
437 and 0.05 for the upward derivative. To aid in the geological interpretation of the results, we
438 converted the estimated upward source coordinates z_o to depths below the surface of the Earth.
439 We did so by subtracting the estimated z_o from the interpolated topographic height of the
440 Shuttle Radar Topography Mission (SRTM; [Earth Resources Observation And Science \(EROS\)](#)
441 [Center, 2017](#)). The estimated positions and structural indices are shown in Figure 7.

442 The estimated source positions shown in Figure 7 highlight the NE-SW lineaments as well
443 as some of the more dipolar anomalies. The lineaments are estimated with a mix of $\eta = 1$,
444 $\eta = 2$, and $\eta = 3$. The southernmost lineament is mostly estimated with $\eta = 1$ and depths
445 suggesting that it does not outcrop in its southernmost parts (depths of 400 m to 600 m), which is
446 consistent with the geologic information in Figure 6a. The southernmost part of this lineament,

in particular, has an estimated $\eta = 3$, which is known to happen for deeper dykes in our synthetic data tests (Section 3.5). Conversely, the northernmost part of the lineament has a larger prevalence of $\eta = 1$ with shallower depths which coincide with a known dyke outcrop. Other known dyke outcrops coincide with estimated sources with $\eta = 1$, however their depths range from 100 m to 300 m. This may be caused by an excess of smoothing in the vertical derivative or effects of noise in the estimated coordinates. The lineaments in the northwestern part of the region are also highlighted by estimated sources. However, their structural indices are a mix of $\eta = 2$ and $\eta = 3$, suggesting deeper sources. This is inline with the geologic information, which includes no outcrops of linear structures in the area.

The dipolar anomalies are associated with post-collisional and alkaline intrusions, many of which are also cut by known outcropping dykes or have known dykes with magnetic signals that significantly overlap with the dipolar anomalies. The Euler inversion estimated structural indices for them range from $\eta = 2$ to $\eta = 3$. We have highlighted four dipolar anomalies, marked as A, B, C, and D in Figure 7, to aid in our discussion.

- **Anomaly A:** Has a reversed polarity and linear feature to its north that is not associated with any known dyke outcrop. The linear feature is highlighted by Euler inversion estimates with $\eta = 1$ and depth of 300 m to 400 m, which can be interpreted as a non-outcropping dyke. The dipolar anomaly itself has Euler inversion solutions with $\eta = 3$ and depth of 1000 m to 2000 m. The solutions in the centre of the anomaly present a shallower depth than the solutions to the north and south of the anomaly centre. From the results on synthetic data in Section 3.5, we can interpret the depth range to be caused by the moving window procedure and the effect of interfering sources. The depth to the centre of the anomaly source is likely close to 1000 m.
- **Anomaly B:** The dipolar anomaly is likely associated with a non-outcropping portion of the post-collisional magmatism. The anomaly is cut by several NE-SW linear features, some of which overlap with known dyke outcrops. The linear feature to the north is associated with Euler inversion results with $\eta = 1$ and depths ranging from 300 m to 600 m, suggesting a non-outcropping dyke. At the centre of the anomaly are Euler inversion

estimates with $\eta = 3$ and depth estimate of approximately 1400 m. The Euler inversion solutions surrounding these central solutions are likely caused by interference from other sources.

- **Anomaly C:** A dipolar anomaly associated with an outcropping portion of the post-collisional magmatism. There is a known outcropping dyke to the south of the anomaly, which is associated with Euler inversion estimates with $\eta = 1$ and depths ranging from 500 m to 1000 m. These depth estimates are likely overestimated because of the interference of the dipolar anomaly. The main anomaly has Euler inversion solutions with $\eta = 2$ and $\eta = 3$ and depths varying from 1400 m to 1800 m. There is no clear indication of which of these estimates is more reliable.
- **Anomaly D:** A small dipolar anomaly associated with an outcropping alkaline intrusion. The Euler inversion estimates have $\eta = 3$ and depths 1700 m to 2000 m. There are known outcropping dykes around the main intrusion but they have no discernible magnetic anomalies and no Euler inversion solutions associated with them.

Overall, the Euler inversion solutions in Figure 7 are consistent with the known geology in Figure 6a. The main linear features are mostly associated with Euler inversion estimates with $\eta = 1$ and shallow depths, particularly where known dyke outcrops are located. Deeper linear features are estimated with $\eta = 2$ and $\eta = 3$, which is consistent with the synthetic data results (Section 3.5). The dipolar anomalies have consistent Euler inversion estimates with $\eta = 3$ when they are well isolated from interfering sources. Otherwise, they are estimated with a mix of structural indices and depths, as was demonstrated in Section 3.5.

4 Conclusion

Euler deconvolution is a widely used method for locating the sources of potential-field data, but under-performs in real-world scenarios due to its dependence on the chosen value of the structural index η and its sensitivity to high-frequency noise and signal overlap. We have developed a new method to solve Euler's homogeneity equation for the source position, base

501 level, and integer structural index, which we call *Euler inversion*. Unlike Euler deconvolution,
502 Euler inversion is also able to estimate the predicted field and its three spatial derivatives,
503 as well as assign different weights to each type of data. The Euler inversion algorithm is
504 computationally efficient because most of the large matrices involved in the computations are
505 diagonal or block-diagonal. We found that, in practice, the computation time of Euler inversion
506 and Euler deconvolution are on the same order of magnitude.

507 Tests on synthetic data show that Euler inversion outperforms Euler deconvolution and
508 finite-difference Euler deconvolution (a variant that estimates η but does not rely on second-
509 order derivatives) in terms of robustness to random noise and interfering sources inside the data
510 window. Our tests also show that the estimated z_o coordinate is correlated with the structural
511 index, as is the case for Euler deconvolution. We have also found that the data misfit from
512 Euler inversion is minimal when the correct structural index is used. This led us to develop
513 an algorithm for estimating the best integer structural index based on the data misfit. A test
514 on complex synthetic data from a model of dykes and dipoles with overlapping signals shows
515 that Euler inversion is able to estimate the structural index and position of the sources within
516 expected error bounds when the signal overlap is not larger than the data window. For deeper
517 dykes in particular, Euler inversion was not able to estimate the correct $\eta = 1$, leading to an
518 overestimation of the depths.

519 We applied Euler inversion to an aeromagnetic dataset from Rio de Janeiro, Brazil, to analyse
520 its performance under real-world scenarios. Euler inversion was able to locate the NE-SW linear
521 features in the data with an $\eta = 1$ which are associated with known dyke outcrops. For the
522 deeper linear features, Euler inversion was not able to estimate the correct $\eta = 1$. Some of
523 the dipolar anomalies present in the data were picked out with $\eta = 3$, while the sources with a
524 large signal overlap with other features provided a mix of $\eta = 2$ and $\eta = 3$. These results are
525 consistent with the synthetic data tests and show the benefits and limitations of the proposed
526 method.

527 Euler inversion outperforms other Euler-based methods in most cases. However, it still
528 suffers from some of the same limitations. While Euler inversion is less sensitive to signal

overlap, it still fails to correctly estimate the position and structural index when the overlap is large. The windowing procedure still generates a large amount of spurious solutions which need to be filtered out. This could be improved with techniques like the source detection method proposed by Castro et al. (2020), for example. Euler inversion can also be coupled with other inverse problems by following our methodology to add Euler's equation as a non-linear constraint. This could help with issues of non-uniqueness and stability in traditional 3D inverse problems in potential-field methods.

Open research

The Python source code and data that were used to produce all results and figures presented here are available at <https://github.com/compgeolab/euler-inversion> and <https://doi.org/10.6084/m9.figshare.26384140> (Uieda et al., 2024) under the CC-BY license and the MIT license. This study made use of the following open-source scientific software: matplotlib (Hunter, 2007) and PyGMT (Tian et al., 2024) for generating figures and maps, Numpy (Harris et al., 2020) and Scipy (Virtanen et al., 2020) for linear algebra, Pandas for manipulating tabular data (McKinney, 2010; The pandas development team, 2024), GeoPandas for reading and plotting shapefiles (den Bossche et al., 2024), pyproj for data projection (Snow et al., 2024), xarray (Hoyer and Hamman, 2017) for working with gridded data, Verde (Uieda, 2018) for moving windows and interpolation, and Harmonica (Fatiando a Terra Project et al., 2023) for potential-field data processing and modeling. The aeromagnetic and geologic data are available from Serviço Geológico do Brasil (<https://geosgb.sgb.gov.br>) under a CC-BY-NC license. The magnetic data are part of survey 1038 “Projeto Aerogeofísico São Paulo – Rio de Janeiro”. Both are also available in our source code and data archive (Uieda et al., 2024).

Acknowledgements

We are indebted to the developers and maintainers of the open-source software without which this work would not have been possible. LU would like to thank Prof. Spiros Pagiatakis for

554 being an incredible instructor and teaching him the mathematics which formed the foundations
555 of this work during his undergraduate exchange at York University. LU was supported in part
556 by start-up grant PRPI 22.1.09345.01.2 from Universidade de São Paulo. GFSJ was supported
557 by scholarship 2021/08379-5 from the Fundação de Amparo à Pesquisa do Estado de São Paulo
558 (FAPESP). The opinions, hypotheses, and conclusions or recommendations expressed in this
559 material are the responsibility of the authors and do not necessarily reflect the views of FAPESP.

560 CRediT author contributions

561 **Leonardo Uieda:** Conceptualisation, Data curation, Formal analysis, Investigation, Methodology,
562 Project administration, Resources, Software, Supervision, Visualisation, Writing original
563 draft. **Gelson Ferreira Souza-Junior:** Data curation, Formal analysis, Resources, Software,
564 Visualisation, Writing - original draft, Writing - review & editing. **India Uppal:** Data curation,
565 Formal analysis, Investigation, Software, Writing - review & editing. **Vanderlei Coelho**
566 **Oliveira Jr.:** Conceptualisation, Methodology, Writing - review & editing.

567 References

- 568 Almeida, J., Dios, F., Mohriak, W., Valeriano, C., Heilbron, M., Eirado, L., and Tomazzoli,
569 E. (2013). Pre-rift tectonic scenario of the eo-cretaceous gondwana break-up along se brazil
570 sw africa insights from tholeiitic mafic dykes swarms. In *Geological Society, London, Special*
571 *Publications*, volume 369, pages 11–40. Geological Society of London.
- 572 Aster, R. C., Borchers, B., and Thurber, C. H. (2018). *Parameter estimation and inverse*
573 *problems*. Elsevier.
- 574 Castro, F. R., Oliveira, S. P., de Souza, J., and Ferreira, F. J. F. (2020). Constraining euler
575 deconvolution solutions through combined tilt derivative filters. *Pure and Applied Geophysics*,
576 177(10):48834895. doi:[10.1007/s00024-020-02533-w](https://doi.org/10.1007/s00024-020-02533-w). URL <http://dx.doi.org/10.1007/s00024-020-02533-w>.
- 577 Dantas, M. E., Moraes, J. M., Ferrassoli, M. A., Jorge, M. d. Q., and Hilquias, V. A. (2017).

- 579 *Geodiversidade do estado do Rio de Janeiro*. CPRM. URL <https://rigeo.sgb.gov.br/handle/doc/20479>.
- 580
- 581 den Bossche, J. V., Jordahl, K., Fleischmann, M., Richards, M., McBride, J., Wasserman,
582 J., Badaracco, A. G., Snow, A. D., Ward, B., Tratner, J., Gerard, J., Perry, M., cjfqf,
583 Hjelle, G. A., Taves, M., ter Hoeven, E., Cochran, M., Bell, R., rraymondgh, Bartos, M.,
584 Roggemans, P., Culbertson, L., Caria, G., Tan, N. Y., Eubank, N., sangarshanan, Flavin,
585 J., Rey, S., and Gardiner, J. (2024). geopandas/geopandas: v1.0.1 [software]. Zenodo.
586 doi:[10.5281/ZENODO.12625316](https://doi.org/10.5281/ZENODO.12625316).
- 587 Earth Resources Observation And Science (EROS) Center (2017). Shuttle radar topography
588 mission (srtm) 1 arc-second global. doi:[10.5066/F7PR7TFT](https://doi.org/10.5066/F7PR7TFT). URL https://www.usgs.gov/carters/eros/science/usgs-eros-archive-digital-elevation-shuttle-radar-topography-mission-srtm-1-arc?qt-science_center_objects=0#qt-science_center_objects.
- 589
- 590
- 591 Egydio-Silva, M., Vauchez, A., Raposo, M., Bascou, J., and Uhlein, A. (2005). Deformation
592 regime variations in an arcuate transpressional orogen (ribeira belt, se brazil) imaged by
593 anisotropy of magnetic susceptibility in granulites. *Journal of Structural Geology*, 27:1750–
594 1764. doi:[10.1016/j.jsg.2005.03.010](https://doi.org/10.1016/j.jsg.2005.03.010).
- 595 Fatiando a Terra Project, Esteban, F. D., Li, L., Oliveira Jr, V. C., Pesce, A., Shea, N., Soler,
596 S. R., Tankersley, M., and Uieda, L. (2023). Harmonica v0.6.0: Forward modeling, inversion,
597 and processing gravity and magnetic data [Software]. Zenodo. doi:[10.5281/zenodo.7690145](https://doi.org/10.5281/zenodo.7690145).
- 598 FitzGerald, D., Reid, A., and McInerney, P. (2004). New discrimination techniques for euler de-
599 convolution. *Computers & Geosciences*, 30(5):461469. doi:[10.1016/j.cageo.2004.03.006](https://doi.org/10.1016/j.cageo.2004.03.006). URL
600 <http://dx.doi.org/10.1016/j.cageo.2004.03.006>.
- 601 Florio, G. and Fedi, M. (2013). Multiridge euler deconvolution. *Geophysical Prospecting*,
602 62(2):333351. doi:[10.1111/1365-2478.12078](https://doi.org/10.1111/1365-2478.12078). URL <http://dx.doi.org/10.1111/1365-2478.12078>.
- 603
- 604 Florio, G., Fedi, M., and Pateka, R. (2014). On the estimation of the structural index from
605 low-pass filtered magnetic data. *GEOPHYSICS*, 79(6):J67J80. doi:[10.1190/geo2013-0421.1](https://doi.org/10.1190/geo2013-0421.1).
- 606 Gerovska, D., Stavrev, P., and Araúzo-Bravo, M. J. (2005). Finite-difference euler deconvolution

- 607 algorithm applied to the interpretation of magnetic data from northern bulgaria. *pure and*
608 *applied geophysics*, 162(3):591608. doi:[10.1007/s00024-004-2623-1](https://doi.org/10.1007/s00024-004-2623-1). URL <http://dx.doi.org/10.1007/s00024-004-2623-1>.
- 610 Harris, C. R., Millman, K. J., van der Walt, S. J., Gommers, R., Virtanen, P., Cournapeau, D.,
611 Wieser, E., Taylor, J., Bergstra, J., Smith, N. J., Kern, R., Picus, M., Hoyer, S., van Kerkwijk,
612 M. H., Brett, M., Haldane, A., Del Río, J., Wiebe, M., Peterson, P., Gérard-Marchant, P.,
613 Sheppard, K., Reddy, T., Weckesser, W., Abbasi, H., Gohlke, C., and Oliphant, T. E. (2020).
614 Array programming with NumPy [software]. *Nature*, 585(7825):357–362. doi:[10.1038/s41586-020-2649-2](https://doi.org/10.1038/s41586-020-2649-2).
- 616 Heilbron, M., Eirado, L., and Almeida, J. (2016). Mapa geológico e de recursos minerais do
617 estado do rio de janeiro. Programa Geologia do Brasil (PGB), Mapas Geológicos Estaduais.
618 Escala 1:400.000.
- 619 Heilbron, M. and Machado, N. (2003). Timing of terrane accretion in the
620 neoproterozoic-eopaleozoic ribeira orogen (se brazil). *Precambrian Research*, 125(1-2):87–112.
621 doi:[10.1016/S0301-9268\(03\)00082-2](https://doi.org/10.1016/S0301-9268(03)00082-2).
- 622 Heilbron, M., Silva, L. G. d. E., Almeida, J. C. H. d., Tupinambá, M., Peixoto, C., Valeriano,
623 C. d. M., Lobato, M., Rodrigues, S. W. d. O., Ragatky, C. D., Silva, M. A., Monteiro, T.,
624 Freitas, N. C. d., Miguens, D., and Girão, R. (2020). Proterozoic to ordovician geology and
625 tectonic evolution of rio de janeiro state, se-brazil: insights on the central ribeira orogen
626 from the new 1:400,000 scale geologic map. *Brazilian Journal of Geology*, 50(2):e20190099.
627 doi:[10.1590/2317-4889202020190099](https://doi.org/10.1590/2317-4889202020190099).
- 628 Heilbron, M., Valeriano, C. M., Tassinari, C. C. G., Almeida, J., Tupinambá, M., Siga, O., and
629 Trouw, R. (2008). Correlation of neoproterozoic terranes between the ribeira belt, se brazil
630 and its african counterpart: comparative tectonic evolution and open questions. *Geological
631 Society, London, Special Publications*, 294(1):211–237. doi:[10.1144/SP294.12](https://doi.org/10.1144/SP294.12).
- 632 Hoyer, S. and Hamman, J. (2017). xarray: N-D labeled arrays and datasets in Python [software].
633 *Journal of Open Research Software*, 5(1). doi:[10.5334/jors.148](https://doi.org/10.5334/jors.148).
- 634 Huang, L., Zhang, H., Li, C., and Feng, J. (2022). Ratioeuler deconvolution and its applications.

- 635 *Geophysical Prospecting*, 70(6):10161032. doi:[10.1111/1365-2478.13201](https://doi.org/10.1111/1365-2478.13201). URL <http://dx.doi.org/10.1111/1365-2478.13201>.
- 636
- 637 Huang, L., Zhang, H., Sekelani, S., and Wu, Z. (2019). An improved tilt-euler deconvolu-
- 638 tion and its application on a fe-polymetallic deposit. *Ore Geology Reviews*, 114:103114.
- 639 doi:[10.1016/j.oregeorev.2019.103114](https://doi.org/10.1016/j.oregeorev.2019.103114). URL <http://dx.doi.org/10.1016/j.oregeorev.2019.103114>.
- 640
- 641 Hunter, J. D. (2007). Matplotlib: A 2d graphics environment [software]. *Computing in Science*
- 642 & Engineering, 9(3):90–95. doi:[10.1109/MCSE.2007.55](https://doi.org/10.1109/MCSE.2007.55).
- 643 McKinney, W. (2010). Data structures for statistical computing in python. In *Proceedings of the*
- 644 *9th Python in Science Conference*, SciPy, page 5661. SciPy. doi:[10.25080/majora-92bf1922-00a](https://doi.org/10.25080/majora-92bf1922-00a). URL <http://dx.doi.org/10.25080/Majora-92bf1922-00a>.
- 645
- 646 Meira, V. T., GarciaCasco, A., Hyppolito, T., Juliani, C., and Schorscher, J. H. D. (2019).
- 647 Tectonometamorphic evolution of the central ribeira belt, brazil: A case of late neoproterozoic
- 648 intracontinental orogeny and flow of partially molten deep crust during the assembly of west
- 649 gondwana. *Tectonics*, 38:3182–3209. doi:[10.1029/2018TC004959](https://doi.org/10.1029/2018TC004959).
- 650
- 651 Meira, V. T., GarciaCasco, A., Juliani, C., Almeida, R. P., and Schorscher, J. H. D. (2015).
- 652 The role of intracontinental deformation in supercontinent assembly: Insights from the ribeira
- 653 belt, southeastern brazil (neoproterozoic western gondwana). *Terra Nova*, 27(3):206–217.
- 654 doi:[10.1111/ter.12149](https://doi.org/10.1111/ter.12149).
- 655
- 656 Melo, F. F. and Barbosa, V. C. (2020). Reliable euler deconvolution estimates throughout
- 657 the vertical derivatives of the total-field anomaly. *Computers & Geosciences*, 138:104436.
- 658 doi:[10.1016/j.cageo.2020.104436](https://doi.org/10.1016/j.cageo.2020.104436).
- 659
- 660 Melo, F. F. and Barbosa, V. C. F. (2018). Correct structural index in euler deconvolution
- 661 via base-level estimates. *GEOPHYSICS*, 83(6):J87J98. doi:[10.1190/geo2017-0774.1](https://doi.org/10.1190/geo2017-0774.1). URL
- 662 <http://dx.doi.org/10.1190/geo2017-0774.1>.
- 663
- 664 Melo, F. F., Barbosa, V. C. F., Uieda, L., Oliveira Jr., V. C., and Silva, J. B. C. (2013).
- 665 Estimating the nature and the horizontal and vertical positions of 3d magnetic sources using
- 666 euler deconvolution. *GEOPHYSICS*, 78(6):J87J98. doi:[10.1190/geo2012-0515.1](https://doi.org/10.1190/geo2012-0515.1). URL <http://dx.doi.org/10.1190/geo2012-0515.1>.
- 667

- 663 //dx.doi.org/10.1190/geo2012-0515.1.
- 664 Pateka, R., Richter, F., Karcol, R., Brazda, K., and Hajach, M. (2009). Regularized deriva-
665 tives of potential fields and their role in semiautomated interpretation methods. *Geophysical*
666 *Prospecting*, 57(4):507516. doi:10.1111/j.1365-2478.2008.00780.x.
- 667 Reid, A. B., Allsop, J. M., Granser, H., Millett, A. J., and Somerton, I. W. (1990). Magnetic
668 interpretation in three dimensions using Euler deconvolution. *GEOPHYSICS*, 55(1):80–91.
669 doi:10.1190/1.1442774.
- 670 Reid, A. B., Ebbing, J., and Webb, S. J. (2014). Avoidable euler errors the use and abuse
671 of euler deconvolution applied to potential fields. *Geophysical Prospecting*, 62(5):11621168.
672 doi:10.1111/1365-2478.12119. URL <http://dx.doi.org/10.1111/1365-2478.12119>.
- 673 Reid, A. B. and Thurston, J. B. (2014). The structural index in gravity and magnetic interpre-
674 tation: Errors, uses, and abuses. *GEOPHYSICS*, 79(4):J61J66. doi:10.1190/geo2013-0235.1.
675 URL <http://dx.doi.org/10.1190/geo2013-0235.1>.
- 676 Ruddock, K. A., Slack, H. A., and Sheldon, B. (1966). Method for determining depth and falloff
677 rate of subterranean magnetic disturbances utilizing a plurality of magnetometers. US Patent
678 3,263,161.
- 679 Saleh, S. and Pateka, R. (2012). Applying the regularized derivatives approach in euler
680 deconvolution and modeling geophysical data to estimate the deep active structures for
681 the northern red sea rift region, egypt. *Contributions to Geophysics and Geodesy*, 42(1).
682 doi:10.2478/v10126-012-0003-x. URL <http://dx.doi.org/10.2478/v10126-012-0003-x>.
- 683 Salem, A. and Ravat, D. (2003). A combined analytic signal and euler method
684 (aneul) for automatic interpretation of magnetic data. *GEOPHYSICS*, 68(6):19521961.
685 doi:10.1190/1.1635049. URL <http://dx.doi.org/10.1190/1.1635049>.
- 686 Salem, A., Smith, R., Williams, S., Ravat, D., and Fairhead, D. (2007). Generalized magnetic
687 tilteuler deconvolution. In *SEG Technical Program Expanded Abstracts 2007*, page 790794.
688 Society of Exploration Geophysicists. doi:10.1190/1.2792530. URL <http://dx.doi.org/10.1190/1.2792530>.
- 689 Silva, J. B. C. and Barbosa, V. C. F. (2003). 3d euler deconvolution: Theoretical basis for au-

- 691 tomatically selecting good solutions. *GEOPHYSICS*, 68(6):19621968. doi:[10.1190/1.1635050](https://doi.org/10.1190/1.1635050).
- 692 URL <http://dx.doi.org/10.1190/1.1635050>.
- 693 Silva, J. B. C., Barbosa, V. C. F., and Medeiros, W. E. (2001). Scattering, symmetry, and
694 bias analysis of sourceposition estimates in euler deconvolution and its practical implications.
695 *GEOPHYSICS*, 66(4):11491156. doi:[10.1190/1.1487062](https://doi.org/10.1190/1.1487062).
- 696 Snow, A. D., Whitaker, J., Cochran, M., Miara, I., den Bossche, J. V., Mayo, C., Lucas, G.,
697 Cochrane, P., de Kloe, J., Karney, C., Shaw, J. J., Filipe, Ouzounoudis, G., Dearing, J.,
698 Lostis, G., Hoesel, D., Couwenberg, B., Jurd, B., Gohlke, C., Schneck, C., McDonald, D.,
699 Itkin, M., May, R., de Bittencourt, H., Little, B., Rahul, P. S., Eubank, N., Neil, and Taves,
700 M. (2024). pyproj4/pyproj: 3.7.0 release [software]. *Zenodo*. doi:[10.5281/ZENODO.13864781](https://doi.org/10.5281/ZENODO.13864781).
- 701 Soler, S. R. and Uieda, L. (2021). Gradient-boosted equivalent sources. *Geophysical Journal
702 International*, 227(3):17681783. doi:[10.1093/gji/ggab297](https://doi.org/10.1093/gji/ggab297). URL <http://dx.doi.org/10.1093/gji/ggab297>.
- 703 Stavrev, P. and Reid, A. (2007). Degrees of homogeneity of potential fields and structural
704 indices of euler deconvolution. *GEOPHYSICS*, 72(1):L1L12. doi:[10.1190/1.2400010](https://doi.org/10.1190/1.2400010). URL
705 <http://dx.doi.org/10.1190/1.2400010>.
- 706 The pandas development team (2024). pandas-dev/pandas: Pandas [software]. *Zenodo*.
707 doi:[10.5281/ZENODO.13819579](https://doi.org/10.5281/ZENODO.13819579).
- 708 Thompson, D. T. (1982). Euldpf: a new technique for making computer-assisted depth esti-
709 mates from magnetic data. *Geophysics*, 47(1):31–37. doi:[10.1190/1.1441278](https://doi.org/10.1190/1.1441278).
- 710 Thompson, R. N., Gibson, S. A., Mitchell, J. G., Dickin, A. P., Leonardos, O. H., Brod, J. A.,
711 and Greenwood, J. C. (1998). Migrating CretaceousEocene Magmatism in the Serra do Mar
712 Alkaline Province, SE Brazil: Melts from the Deflected Trindade Mantle Plume? *Journal of
713 Petrology*, 39(8):1493–1526. doi:[10.1093/petroj/39.8.1493](https://doi.org/10.1093/petroj/39.8.1493).
- 714 Tian, D., Uieda, L., Leong, W. J., Fröhlich, Y., Schlitzer, W., Grund, M., Jones, M., Toney, L.,
715 Yao, J., Magen, Y., Jing-Hui, T., Materna, K., Belem, A., Newton, T., Anant, A., Ziebarth,
716 M., Quinn, J., and Wessel, P. (2024). Pygmt: A python interface for the generic mapping
717 tools [software]. doi:[10.5281/ZENODO.3781524](https://doi.org/10.5281/ZENODO.3781524).

- 719 Trouw, R., Heilbron, M., Ribeiro, A., Paciullo, F., Valeriano, C., Almeida, J., Tupinambá, M.,
720 and Andreis, R. (2000). The central segment of the ribeira belt. In Cordani, U., Milani, E.,
721 Thomaz Filho, A., and Campos, D., editors, *Geotectonics of South America*, pages 297–310.
722 31st International Geological Congress (IGC), Special Publication.
- 723 Uieda, L. (2018). Verde: Processing and gridding spatial data using Green's functions [software].
724 *Journal of Open Source Software*, 3(29):957. doi:[10.21105/joss.00957](https://doi.org/10.21105/joss.00957).
- 725 Uieda, L., Oliveira, V., and Barbosa, V. (2013). Modeling the earth with fatiando a
726 terra. In *Proceedings of the 12th Python in Science Conference*, SciPy, page 9298. SciPy.
727 doi:[10.25080/majora-8b375195-010](https://doi.org/10.25080/majora-8b375195-010). URL <http://dx.doi.org/10.25080/Majora-8b375195-010>.
- 728 Uieda, L., Oliveira, V. C., and Barbosa, V. C. F. (2014). Geophysical tutorial: Euler decon-
729 volution of potential-field data. *The Leading Edge*, 33(4):448450. doi:[10.1190/tle33040448.1](https://doi.org/10.1190/tle33040448.1).
730 URL <http://dx.doi.org/10.1190/tle33040448.1>.
- 731 Uieda, L., Souza-Junior, G. F., Uppal, I., and Oliveira Jr., V. C. (2024). Supplementary
732 material for “Euler inversion: Locating sources of potential-field data through inversion of
733 Eulers homogeneity equation” [Dataset]. doi:[10.6084/m9.figshare.26384140](https://doi.org/10.6084/m9.figshare.26384140).
- 734 Valeriano, C., Tupinambá, M., Simonetti, A., Heilbron, M., Almeida, J., and Eirado Silva,
735 L. (2011). U-pb la-mc-icpms geochronology of cambro-ordovician post-collisional gran-
736 ites of the ribeira belt, southeast brazil: terminal brasiliense magmatism in central
737 gondwana supercontinent. *Journal of South American Earth Sciences*, 32(4):416–428.
738 doi:[10.1016/j.jsames.2011.03.003](https://doi.org/10.1016/j.jsames.2011.03.003).
- 739 Van Huffel, S. and Vandewalle, J. (1991). *The Total Least Squares Problem: Computational
740 Aspects and Analysis*. Society for Industrial and Applied Mathematics. ISBN 9781611971002.
741 doi:[10.1137/1.9781611971002](https://doi.org/10.1137/1.9781611971002).
- 742 Vanícek, P. and Krakiwsky, E. (1986). *Geodesy: The Concepts*. Elsevier Science.
- 743 Virtanen, P., Gommers, R., Oliphant, T. E., Haberland, M., Reddy, T., Cournapeau, D.,
744 Burovski, E., Peterson, P., Weckesser, W., Bright, J., van der Walt, S. J., Brett, M., Wilson,
745 J., Millman, K. J., Mayorov, N., Nelson, A. R. J., Jones, E., Kern, R., Larson, E., Carey, C. J.,
746 Polat, I., Feng, Y., Moore, E. W., VanderPlas, J., Laxalde, D., Perktold, J., Cimrman, R.,

- 747 Henriksen, I., Quintero, E. A., Harris, C. R., Archibald, A. M., Ribeiro, A. H., Pedregosa, F.,
748 van Mulbregt, P., and Contributors (2020). SciPy 1.0: Fundamental Algorithms for Scientific
749 Computing in Python [Software]. *Nature Methods*, 17(3):261–272. doi:[10.1038/s41592-019-0686-2](https://doi.org/10.1038/s41592-019-0686-2).
- 751 Wells, D. and Krakiwsky, E. (1971). *The method of least squares*. Number 18. Department of
752 Geodesy and Geomatics Engineering Lecture Notes, University of New Brunswick.